NASA Technical Paper 2898

1989

Modal Control of an Oblique Wing Aircraft

James D. Phillips
Ames Research Center
Moffett Field, California

National Aeronautics and Space Administration

Scientific and Technical Information Division

SYMBOLS

a	damping coefficient for a second-order system
C_ℓ	rolling moment coefficient
C_{ℓ_α}	rolling moment coefficient derivative with respect to angle of attack
e	error signal, difference between command and state
k	control gain or spring coefficient of second-order system
m	number of controls, 3 for the OWRA
n	number of states, 8 for the OWRA
p	body axis perturbation roll rate, radians/second
q	body axis perturbation pitch rate, radians/second
r	body axis perturbation yaw rate, radians/second
s	La Place Transform variable
u	flight direction perturbation velocity, feet/second
U_1	reference condition velocity, feet/second
v_i	eigenvectors
α	aircraft angle of attack relative to an arbitrary reference axis, usually parallel to the fuselage centerline, degrees
β	sideslip angle, degrees, + nose left of wind vector
δe_L	left elevator, degrees, + trailing edge down
δe_R	right elevator, degrees, + trailing edge down
δr	rudder, degrees, + trailing edge left
ζ	damping ratio
θ	pitch angle, radians
λ_i	eigenvalue
ν_i	complex modal control vector

τ	time constant
ϕ	roll angle, radians, + right bank
ω_n	natural frequency, radians/second

Matrices and Vectors:

C	inverse of 3×3 feed-forward matrix
D	8×8 denominator matrix
F	open-loop 8×8 dynamics matrix
G	open-loop 8×3 control matrix
I	identity matrix
K	3×3 control-gain matrix
L	load or disturbance vector
M	8×3 complex modal control matrix
N	8×8 numerator matrix
P	8×8 second-order transformation matrix
S	3×3 second-order modal control matrix
T	3×8 transformation matrix from natural coordinates to second-order modal coordinates
u	3×1 natural control vector
w	3×1 second-order modal control vector
x	8×1 natural state vector
X	8×8 matrix of eigenvectors
y	3×1 second-order modal state vector
z	3×1 pilot command vector
$\mathbf{\Gamma}$	8×8 second-order modal dynamics matrix
$\mathbf{\Lambda}$	8×8 complex eigenvalue diagonal matrix

ξ	8×1 complex modal state vector
$\mathbf{\Phi}$	null matrix
χ	3×1 integral of modal state vector

Subscripts:

c	control command
d	pseudo-derivative gain
dr	Dutch roll
i	integral gain
p	periodic (second order)
ph	phugoid mode
r	outer roll loop gain
rm	roll mode
sp	short-period mode
spl	spiral mode
0	value at start of control interval

Superscripts:

T	transpose of a square matrix
-1	inverse of a square matrix
$*$	complex conjugate

Acronyms:

$OWRA$	Oblique Wing Research Aircraft
$SISO$	single-input/single-output
$MIMO$	multiple-input/multiple-output
PDF	pseudo-derivative feedback
$P+I$	proportional plus integral control

MODAL CONTROL OF AN OBLIQUE WING AIRCRAFT

James D. Phillips

Ames Research Center

SUMMARY

A linear modal control algorithm is applied to the NASA Oblique Wing Research Aircraft (OWRA). The control law is evaluated using a detailed nonlinear flight simulation. It is shown that the modal control law attenuates the coupling and nonlinear aerodynamics of the oblique wing and remains stable during control saturation caused by large command inputs or large external disturbances. The technique controls each natural mode independently allowing single-input/single-output techniques to be applied to multiple-input/multiple-output systems.

INTRODUCTION

The oblique-wing aircraft configuration, in which the entire wing yaws about a midspan pivot during flight, is a promising but unproven idea. Large reductions in supersonic wave drag and structural weight over symmetrical, variable-sweep aircraft, without the rearward movement of the lift-center with sweep, are theoretically possible. Despite this, the idea had not been tested in hardware for more than 30 years after its proposal because of perceived aeroelastic and flight-control problems. In 1979, the first and only full-size oblique-wing aircraft, the AD-1, was flight-tested by NASA at Dryden Research Center. This vehicle is a low-cost, low-speed research vehicle which demonstrates that the aeroelastic and control problems are not insurmountable. It remains to be shown, however, that these problems can be overcome at supersonic speeds where the configuration's benefits accrue.

To that end, NASA initiated a program in 1984 to design, build, and flight-test a *high-speed*, oblique-wing research aircraft, designated the Oblique Wing Research Aircraft (OWRA). The proposal is to put an oblique wing on NASA's F-8 Digital Fly-By-Wire Aircraft. This takes advantage of the original F-8 wing mount, which adjusts the wing's incidence in flight, and the existing digital flight control-system which will expedite control-system development. Preliminary design of this aircraft is complete.

NASA has two broad goals in designing the OWRA. The first goal is to flight-test a research aircraft to demonstrate the theoretical advantages of oblique wings and to uncover possible problems with the concept. This goal is concerned with the specific design details of a single aircraft. The second broad goal is to develop useful technology for designing *future* oblique-wing aircraft. This second goal is much more general and involves developing technology applicable to all oblique

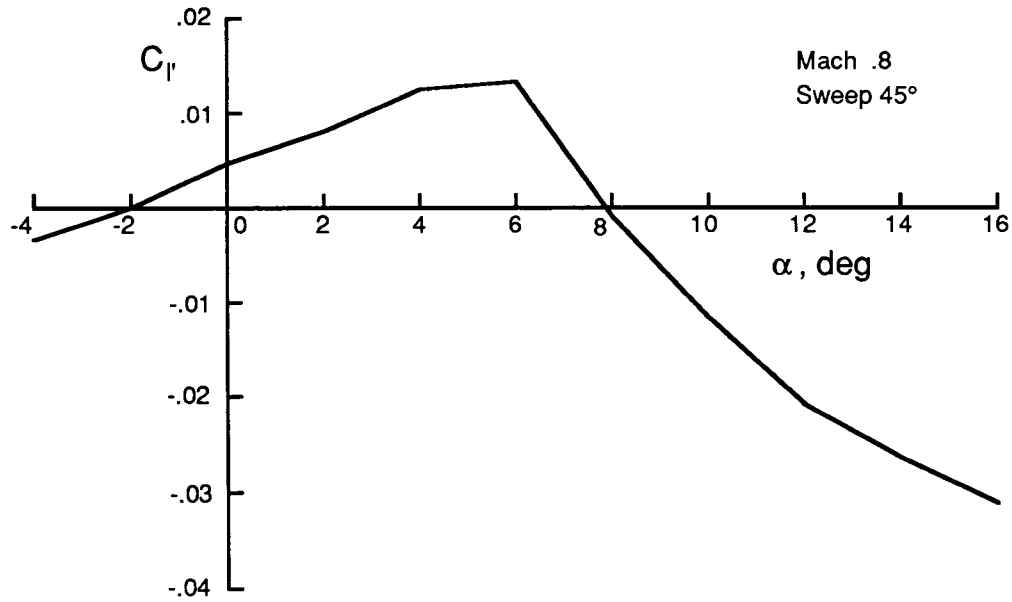

Figure 1. – Rolling moment coefficient versus angle of attack.

wing aircraft. This paper addresses the second broad goal in the area of flight dynamics and control, specifically the development of a control-system design technique applicable to oblique-wing aircraft.

Control-system design for oblique-wing aircraft is difficult. The longitudinal and lateral motions are strongly coupled in contrast to symmetric configurations. The most difficult coupling to deal with is that, with increasing angle of attack, an oblique-wing aircraft rolls strongly into the forward-swept wing because of the normal tip-loading behavior of swept wings (think of the oblique wing as one-half of a symmetrically swept wing). To make matters worse, the boundary layer builds up in the direction of the aft swept wing, so the aft wing stalls first, producing a strong rolling moment in the opposite direction from its prestall behavior.

Figure 1 illustrates this with a plot of the rolling moment coefficient, $C_{\ell'}$, versus the angle of attack, α, for the proposed OWRA at Mach 0.8 and 45° sweep. The slope of this curve is the pitch-to-roll coupling derivative, $C_{\ell'_\alpha}$, which, along with $C_{\ell'}$, is zero for symmetric aircraft. The steepness of the slope for low angles of attack represents a strong coupling term, and the sudden change in slope at about 6° as the trailing wing stalls represents a significant nonlinear behavior.

To cope with this nonlinear behavior, all the proposed control systems for the OWRA are robust linear designs. One approach, developed at NASA (refs. 1 and 2), uses a model-following technique, wherein the nonlinear aircraft is "slaved" to follow a desired linear model. Another approach called eigenstructure assignment (ref. 3), in which the aircraft modes and eigenvalues are transformed to decouple them, has been applied to oblique-wing aircraft with limited success (refs. 1 and 4). Finally, a loop-shaping technique, in which allowance is made in the frequency domain for variations in the roots, has been developed and will be implemented on the OWRA (ref. 5).

This paper proposes a different linear-control method based upon decoupled control of the aircraft modes. Throughout this paper I will call this method "modal control," although this term has been applied to other control schemes (ref. 6).

There were four goals for the control system described in this paper. First, because the accepted handling qualities specifications (ref. 7) are in terms of frequency and damping ratio of natural aircraft modes, the control system gains should affect these frequencies and damping ratios without changing the mode shapes, so that valuable insight about the modes (on which the handling qualities specifications are based) is not lost. This direct connection between the control system and the open-loop modes is also important because, in general, the more the closed-loop system differs from the open loop system, the more control power will be required. Second, the new control system should decouple the longitudinal- and lateral-directional aircraft response to be similar to that of a symmetric airplane. Third, since the aircraft is nonlinear, the control system should have zero steady state error to handle model uncertainty and atmospheric disturbances. For example, a steady roll-rate error in response to a step pitch-angle command would not be acceptable for the OWRA. Fourth, the control system should remain stable and recover from large control inputs and external disturbances which can reasonably be expected in service and which may cause the controls to be rate-limited or position-limited.

The modal theory developed in this paper was implemented in a computer simulation of the OWRA at one worst-case flight condition where the aerodynamics are particularly nonlinear. It should be noted that to apply this control system throughout the flight envelope will require calculating control gains for many different flight conditions and gain scheduling in between. This is a common technique to extend linear control schemes to nonlinear dynamic systems. In addition, note that full-state measurement is assumed to be available to the control system. In most cases, this means that a state observer will have to be developed to fill in missing states not measured directly and to filter measurement noise.

The body of this paper is divided into four sections. The first section describes a general linear modal control theory which can be applied to a large class of dynamic systems. The second section describes the application of the theory to a linear math model of the OWRA as an example and also describes some features of the control design that are unique to the OWRA implementation. Up to this second section in the paper, the OWRA math model has been linear. The third section describes a nonlinear math model of the OWRA used to verify the modal control concept and a new algorithm for handling control saturation. The more realistic nonlinear model results in an unacceptably large roll response so an extra, outer feedback loop is added. The fourth section describes dynamic test cases used to validate the model and control system and describes an incidental conclusion regarding control-limiting specific to oblique wings.

It should be observed that the control-system improvements described herein range from general to OWRA-specific. The assumptions and limitations (where known) for each new idea will be explained.

MODAL CONTROL THEORY

Modal control begins with the classical linear modal decomposition of the natural dynamic system. Selected eigenvalues are then moved to desirable damping and frequency without coupling the eigenvectors. The resulting eigenvectors are then combined to produce acceptable responses to the pilot's inputs.

This simple idea is complicated by the fact that most real control systems have fewer controls than states. This means that only as many states (or linear combinations of the states) as controls can be explicitly specified as a function of time. The rest of the states are determined in time by the closed-loop dynamics. The approach here is to control independently as many natural *modes* as there are controls. The remaining modes may be ignored in the initial control design, either because they are sufficiently stable naturally or because they are an order of magnitude slower and can be controlled by cascaded outer feedback loops. For example, in the flight-control design of a conventional transport, the structural modes of the wing are frequently ignored because of their order-of-magnitude more rapid, yet stable, response. Even if the structural modes become a problem (say if the wings are very slender), they can still be controlled by a separate feedback loop because of the large difference in time response between the structural modes and the flight-dynamic modes.

Cascaded feedback loops are preferable (when they can be used) to true multiple-input/multiple-output (MIMO) control schemes because they allow the control designer to design each feedback loop independently. This means that separate single-input/single-output (SISO) techniques can be used for each feedback loop. Also, classical SISO techniques, which have no obvious MIMO implementation, can be used. The motivation behind modal control is to find a special coordinate transformation to modal coordinates where SISO techniques can be successfully applied in spite of multiple natural modes which have similar time responses.

Many dynamic systems, aircraft in particular, can be described by a linear coupled set of first-order differential equations as follows

$$\dot{\mathbf{x}} = \mathbf{F}\ \mathbf{x} + \mathbf{G}\ \mathbf{u} \tag{1}$$

where $\mathbf{x}$ and $\mathbf{u}$ are the state and control vectors, respectively,

$$\begin{aligned} \mathbf{x} &= [x_1\ x_2\ \cdots x_n]^T \\ \mathbf{u} &= [u_1\ u_2\ \cdots u_m]^T \end{aligned} \tag{2}$$

$\mathbf{F}$ is the square $n \times n$ dynamics matrix, and $\mathbf{G}$ is the $n \times m$ control matrix.

The dynamics matrix, $\mathbf{F}$, can be diagonalized by solving for the roots of the nth-order characteristic polynomial. Assuming distinct roots, each root or eigenvalue is associated with an eigenvector or mode. The original system of equations (eq.(1)) is then diagonalized by a similarity transformation using a matrix made up of the eigenvectors. Mathematically,

$$\dot{\xi} = \mathbf{\Lambda}\ \xi + \mathbf{M}\ \mathbf{u} \tag{3}$$

where if v_i are the eigenvectors of $\mathbf{F}$, then

$$\begin{aligned} \mathbf{X} &= [v_1\ v_2\ \cdots v_n] \\ \xi &= \mathbf{X}^{-1}\,\mathbf{x} \\ \mathbf{\Lambda} &= \mathbf{X}^{-1}\mathbf{F}\mathbf{X} \\ \mathbf{M} &= \mathbf{X}^{-1}\mathbf{G} \end{aligned} \tag{4}$$

The special property of this transformation is that $\mathbf{\Lambda}$ is a diagonal matrix with the eigenvalues along the diagonal. This decouples the system into n linear first-order differential equations. Unfortunately, many of these equations will be complex; that is, in general $\mathbf{\Lambda}$ and $\mathbf{M}$ contain complex elements, and cannot be used in real control systems.

However, the characteristic polynomial, $|\lambda\mathbf{I} - \mathbf{\Lambda}| = 0$, can be factored into real roots and complex conjugate pairs. This means that again, assuming nonrepeated roots, there are at most two types of modes: real and second-order. The real modes can be controlled directly; the second-order modes require a transformation to a real system. If we reorder equations (3) such that the equations corresponding to complex conjugate eigenvalues occur in pairs, then each second-order mode representing two equations from (3) can be transformed by a 2×2 matrix, preserving the modal decoupling to 2×2 blocks along the diagonal of the transformed dynamics matrix. Reordering equations (3) does not change the eigenvalues or the eigenvectors. If we define a second-order transformation matrix $\mathbf{P}$ such that

$$\mathbf{y} = \mathbf{P}^{-1}\xi \tag{5}$$

where $\mathbf{P}$ is the identity except that in line with a pair of complex conjugate eigenvalues a special 2×2 matrix is placed on the diagonal, then equations (3) transform to

$$\dot{\mathbf{y}} = \mathbf{\Gamma}\ \mathbf{y} + \mathbf{S}\ \mathbf{u} = \mathbf{\Gamma}\ \mathbf{y} + \mathbf{w} \tag{6}$$

where

$$\begin{aligned} \mathbf{\Gamma} &= \mathbf{P}^{-1}\mathbf{\Lambda}\mathbf{P} \\ \mathbf{S} &= \mathbf{P}^{-1}\mathbf{M} \end{aligned} \tag{7}$$

$\mathbf{\Gamma}$ and $\mathbf{S}$ are now real matrices, $\mathbf{y}$ and $\mathbf{w}$ are real vectors, and $\mathbf{\Gamma}$, $\mathbf{P}$, and $\mathbf{P}^{-1}$ have the structure below with 2×2 matrices occurring for each pair of complex equations.

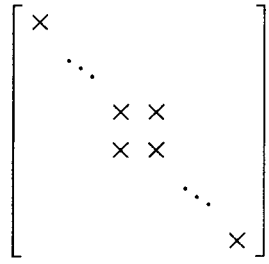

The process and theoretical basis for determining the $\mathbf{P}^{-1}$ matrix is presented next.

A second-order mode from equations (3) represents two equations and and therefore strictly requires two linear combinations of the controls for explicit determination. With a limited number

of controls, it may be necessary (and, as will be shown, satisfactory) to handle each second-order mode with a single linear combination of the available controls. A suitable choice of $\mathbf{P}^{-1}$ will approximately achieve this result.

For a typical second-order mode from equations (3), say at rows p and $p+1$, we have the two equations

$$\begin{bmatrix} \xi_p \\ \xi_{p+1} \end{bmatrix} = \begin{bmatrix} \xi_p \\ \xi_p^* \end{bmatrix} = \begin{bmatrix} \lambda_p & 0 \\ 0 & \lambda_p^* \end{bmatrix} \begin{bmatrix} \xi_p \\ \xi_p^* \end{bmatrix} + \begin{bmatrix} \nu_p \\ \nu_p^* \end{bmatrix} \tag{8}$$

where, since $\mathbf{M}$ can be a full matrix,

$$\begin{aligned} \nu_p &= \nu_p = m_{p1} u_1 + m_{p2} u_2 + \cdots + m_{pm} u_m \\ \nu_{p+1} &= \nu_p^* = m_{p1}^* u_1 + m_{p2}^* u_2 + \cdots + m_{pm}^* u_m \end{aligned} \tag{9}$$

It is shown in appendix A that row $p+1$ is indeed the conjugate of row p.

Each 2×2 matrix from $\mathbf{P}^{-1}$ can be interpreted as a coordinate transformation from the complex conjugate coordinates, ξ_p and ξ_p^*, to two new real coordinates, y_p and y_{p+1}. In some sense, y_p and y_{p+1} still represent the second-order mode, because none of the other eigenvalues or eigenvectors have been changed by this transformation. There are an infinite number of such transformations, but we desire a tranformation which makes one coordinate proportional to the derivative of the other ($y_{p+1} \propto \dot{y}_p$). The resulting 2×2 matrix within $\mathbf{\Gamma}$ will then contain one zero on its diagonal.

If we choose the corresponding 2×2 block within $\mathbf{P}^{-1}$ as follows:

$$\mathbf{P}_p^{-1} = \begin{bmatrix} -\lambda_p^* & -\lambda_p \\ 1 & 1 \end{bmatrix} \tag{10}$$

then equation (8) transforms to

$$\begin{bmatrix} \dot{y}_p \\ \dot{y}_{p+1} \end{bmatrix} = \underbrace{\begin{bmatrix} 0 & -k \\ 1 & -a \end{bmatrix}}_{\mathbf{\Gamma}_p} \begin{bmatrix} y_p \\ y_{p+1} \end{bmatrix} + \underbrace{\begin{bmatrix} -\lambda_p^* & -\lambda_p \\ 1 & 1 \end{bmatrix} \begin{bmatrix} \nu_p \\ \nu_p^* \end{bmatrix}}_{\mathbf{w}} \tag{11}$$

where $\mathbf{\Gamma}_p$ will appear as a 2×2 block on the diagonal of $\mathbf{\Gamma}$ and

$$\mathbf{w} = \begin{bmatrix} w_p \\ w_{p+1} \end{bmatrix} = \begin{bmatrix} -(\lambda_p^* \nu_p + \lambda_p \nu_p^*) \\ \nu_p + \nu_p^* \end{bmatrix} \tag{12}$$

After some algebra it can also be shown that

$$\begin{aligned} k &= \|\lambda_p\|^2 \\ a &= -2 \times \Re\{\lambda_p\} \end{aligned} \tag{13}$$

For stable systems, a is positive.

If we eliminate y_p, equations (11) become

$$\ddot{y}_{p+1} + a\, \dot{y}_{p+1} + k\, y_{p+1} = w_p + \dot{w}_{p+1} \approx w_p \tag{14}$$

This shows the second-order mode y_{p+1} controlled approximately by w_p, a single real combination of the original controls, $\mathbf{u}$. y_{p+1} is controlled exactly by w_p in the steady state. If λ_p and ν_p are considered as vectors in the complex plane (e.g., $z = x + \imath y = (x, y)$), then w_p can be expressed as a cartesian dot product

$$w_p = -2(\lambda_p^* \cdot \nu_p) \tag{15}$$

If we repeatedly use equation (10) for each second-order mode in the $\mathbf{\Lambda}$ matrix, we can build up the matrix, $\mathbf{P}^{-1}$. We can derive the transformation from the original system, equation (1), to the modal system, equation (6), by simply multiplying the two transformations $\mathbf{X}$ and $\mathbf{P}$ to get $\mathbf{T} = \mathbf{XP}$ and then

$$\begin{aligned} \mathbf{y} &= \mathbf{T}^{-1}\mathbf{x} \\ \mathbf{\Gamma} &= \mathbf{T}^{-1}\mathbf{F}\mathbf{T} \\ \mathbf{S} &= \mathbf{T}^{-1}\mathbf{G} \end{aligned} \tag{16}$$

where $\mathbf{T}$, $\mathbf{T}^{-1}$, $\mathbf{\Gamma}$, and $\mathbf{S}$ are real matrices and can hence be used in a real control system.

It should be emphasized that unless there are as many controls as states (a rare luxury), $\mathbf{T}^{-1}$ will be reduced in the row dimension by neglecting modes or combining second-order modes as in equation (14). This must be true so that $\mathbf{S}$ is a square matrix and can be inverted. It is $\mathbf{S}^{-1}$ that is actually used in the real control system.

APPLICATION TO THE OWRA

The theory just described will be applied directly to the OWRA flight dynamics. Each important matrix ($\mathbf{F}$, $\mathbf{G}$, etc.) is provided in full 8×8 numerical form in appendix B. Much can be learned by examining the structure of these matrices.

The reference configuration for this study is the OWRA at 45° sweep, Mach 0.8, and 20,000 ft in level flight. It is modeled by eight linear, perturbation equations with three controls in the form of equation (1). The eight equations are derived from three moment-balance equations, three force-balance equations, and two kinematic equations. The state and control vectors are, respectively,

$$\begin{aligned} \mathbf{x} &= [\,q,\ \alpha,\ u/U_1,\ \theta,\ p,\ r,\ \beta,\ \phi\,]^T \\ \mathbf{u} &= [\,\delta e_L,\ \delta e_R,\ \delta r\,]^T \end{aligned} \tag{17}$$

where p, q, and r are the body axis perturbation roll, pitch, and yaw angular rates; u/U_1, β, and α represent the longitudinal, lateral, and vertical perturbation velocities; and θ and ϕ are the perturbation pitch and roll attitudes. The controls are left elevator, right elevator, and rudder.

Assuming that the inertia coupling is accounted for, the dynamics matrix, $\mathbf{F}$, and the control matrix, $\mathbf{G}$ are given next in symbolic form. See appendix B for actual values for the OWRA at the design condition.

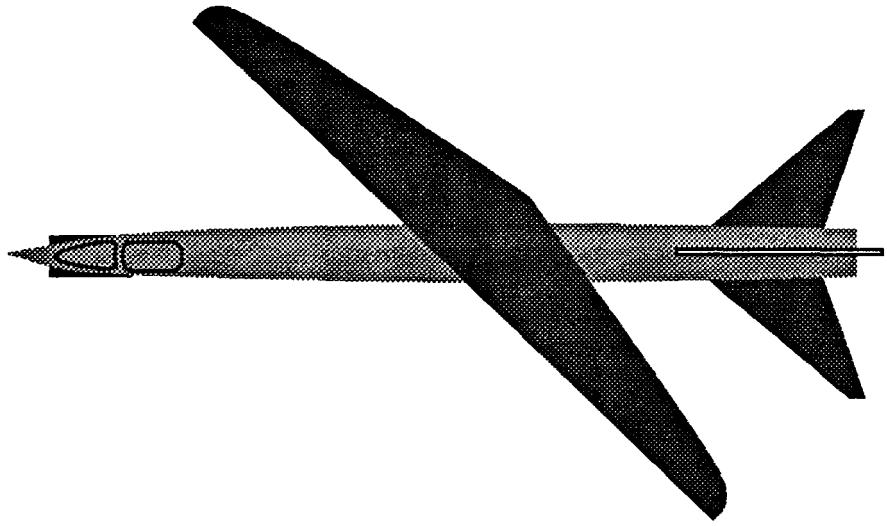

Figure 2. – OWRA at 45° sweep.

$$\mathbf{F} = \begin{bmatrix} M_q & M_w U_1 & 0 & 0 & M_p & M_r & 0 & 0 \\ 1 & Z_w & Z_u & 0 & 0 & 0 & 0 & 0 \\ 0 & X_w & X_u & -g/U_1 & 0 & 0 & 0 & 0 \\ 1 & 0 & 0 & 0 & 0 & 0 & 0 & 0 \\ L_q & L_w U_1 & 0 & 0 & L_p & L_r & L_\beta & 0 \\ 0 & N_w & 0 & 0 & N_p & N_r & N_\beta & 0 \\ 0 & 0 & 0 & 0 & -1 & Y_v & g/U_1 & 0 \\ 0 & 0 & 0 & 0 & 1 & 0 & 0 & 0 \end{bmatrix}$$

$$\mathbf{G} = \begin{bmatrix} M_{\delta e_L} & M_{\delta e_R} & M_{\delta r} \\ Z_{\delta e_L} & Z_{\delta e_R} & Z_{\delta r} \\ X_{\delta e_L} & X_{\delta e_R} & X_{\delta r} \\ 0 & 0 & 0 \\ L_{\delta e_L} & L_{\delta e_R} & L_{\delta r} \\ N_{\delta e_L} & N_{\delta e_R} & N_{\delta r} \\ Y_{\delta e_L} & Y_{\delta e_R} & Y_{\delta r} \\ 0 & 0 & 0 \end{bmatrix} \tag{18}$$

The unusual splitting of the elevator surfaces allows the generation of roll moments as well as conventional pitching moments. This avoids using the highly coupled and nonlinear aileron controls at high sweep. It is also surprisingly effective at generating rolling moments. The horizontal tail is not pivoted with the wing, so its span is comparable to the highly swept wing (fig. 2).

The addition of the left and right ailerons to the control vector would not alter the control problem except for the additional control power available to avoid the nonlinearity of limits or improve response. This is because all five controls are essentially moment controls and therefore

span a vector space of dimension three. Despite five controls, the number of states which can be explicitly determined is only three.

The OWRA has five modes at the design condition, three second order and two real. These are the short-period mode, the phugoid mode, the roll mode, the spiral mode, and the Dutch roll mode. The eigenvalues and corresponding natural frequencies and damping ratios for these modes at the reference condition are

$$\begin{aligned}
\lambda_{sp} &= -1.084 \pm 2.618j \Rightarrow \omega_{n_{sp}} = 2.834,\ \zeta_{sp} = 0.382 \\
\lambda_{ph} &= -0.007 \pm 0.053j \Rightarrow \omega_{n_{ph}} = 0.053,\ \zeta_{ph} = 0.131 \\
\lambda_{rm} &= -2.750 \qquad\qquad \Rightarrow \tau_{rm} = 0.364 \\
\lambda_{spl} &= -0.030 \qquad\qquad \Rightarrow \tau_{spl} = 33.333 \\
\lambda_{dr} &= -0.487 \pm 3.146j \Rightarrow \omega_{n_{dr}} = 3.184,\ \zeta_{dr} = 0.153
\end{aligned} \tag{19}$$

where frequencies are in radians/second and time constants are in seconds.

The values shown above would not be unusual as eigenvalues for a symmetric configuration. We will take advantage of the approximate order of magnitude difference in time response between the two "slow" modes (the spiral and phugoid modes) and the three "fast" modes (the short-period, the roll mode, and the Dutch roll mode). If we succeed in controlling the fast modes, we can stabilize the slow modes with cascaded outer control loops as stated earlier. On the basis of this argument, we will drop the slow-mode equations and thereby reduce the number of motion equations to five.

We now have reduced the number of *modes* to be controlled to the number of available controls (three), but the number of equations is still five because of the two second-order modes. These three modes (eigenvectors) are presented below in polar form with magnitudes normalized to unity and phase-adjusted such that the distinguishing component has zero phase (the magnitude and phase of an eigenvector are not unique). These eigenvectors are quite different from the equivalent modes for a symmetric aircraft. In particular, the roll and pitch components are highly coupled as described in the introduction.

$$v_{sp} = \begin{bmatrix} .353 \angle 96.1^{\circ} \\ .134 \angle 0.0^{\circ} \\ .001 \angle 18.6^{\circ} \\ .125 \angle -16.4^{\circ} \\ .858 \angle -79.7^{\circ} \\ .114 \angle -39.4^{\circ} \\ .046 \angle 36.2^{\circ} \\ .303 \angle 167.8^{\circ} \end{bmatrix} \quad v_{rm} = \begin{bmatrix} -.025 \\ .013 \\ .000 \\ .009 \\ .939 \\ -.011 \\ .001 \\ -.342 \end{bmatrix} \quad v_{dr} = \begin{bmatrix} .100 \angle 87.4^{\circ} \\ .032 \angle 3.2^{\circ} \\ .000 \angle 44.5^{\circ} \\ .031 \angle -11.4^{\circ} \\ .920 \angle 133.3^{\circ} \\ .228 \angle -84.1^{\circ} \\ .074 \angle 0.0^{\circ} \\ .289 \angle 34.5^{\circ} \end{bmatrix} \begin{matrix} q \\ \alpha \\ u/U_1 \\ \theta \\ p \\ r \\ \beta \\ \phi \end{matrix} \tag{20}$$

The symbols at the right side are the components of the natural-state vector.

In a symmetric airplane, the bottom four components of the short-period eigenvector would be zero and the top four components of the Dutch roll and roll-mode eigenvectors would be zero. As can be readily seen, the specified components are far from zero, and in fact, the short-period roll-rate component, p, *is more than twice* the pitch component q.

Applying modal control theory and dropping the phugoid and spiral mode equations after the transformation, we can write five equations for the OWRA at the reference condition in matrix form

$$\dot{\mathbf{y}} = \mathbf{\Gamma}\ \mathbf{y} + \mathbf{S}\ \mathbf{u} = \mathbf{\Gamma}\ \mathbf{y} + \mathbf{w} \tag{21}$$

where

$$\begin{aligned} \mathbf{y} &= \mathbf{T}^{-1}\mathbf{x} = [\, y_{sp_1},\ y_{sp_2},\ y_{rm},\ y_{dr_1},\ y_{dr_2}\,]^T \\ \mathbf{w} &= [\, w_{sp_1},\ w_{sp_2},\ w_{rm},\ w_{dr_1},\ w_{dr_2}\,]^T \end{aligned} \tag{22}$$

and where (see appendix B for the full eight equations)

$$\mathbf{T}^{-1} = \begin{bmatrix} 8.981 & 8.381 & -0.572 & -0.009 & 0.126 & 4.293 & -3.935 & -0.148 \\ 0.043 & 9.150 & 0.085 & -0.003 & -0.116 & -0.240 & -4.882 & 0.019 \\ 3.012 & -7.568 & -0.228 & -0.003 & 1.231 & 4.780 & 12.580 & -0.177 \\ -4.248 & 9.813 & 0.430 & -0.002 & -0.227 & -15.923 & 3.882 & 0.590 \\ -1.344 & -4.273 & 0.081 & 0.002 & -0.004 & -0.649 & 15.628 & -0.015 \end{bmatrix} \begin{matrix} sp_1 \\ sp_2 \\ rm \\ dr_1 \\ dr_2 \end{matrix}$$

$$\mathbf{\Gamma} = \begin{bmatrix} 0 & -8.030 & 0 & 0 & 0 \\ 1 & -2.167 & 0 & 0 & 0 \\ 0 & 0 & -2.750 & 0 & 0 \\ 0 & 0 & 0 & 0 & -10.135 \\ 0 & 0 & 0 & 1 & -0.973 \end{bmatrix} \begin{matrix} sp_1 \\ sp_2 \\ rm \\ dr_1 \\ dr_2 \end{matrix}$$

$$\mathbf{S} = \begin{bmatrix} -1.234 & -1.762 & -0.34704 \\ -0.052 & 0.024 & -0.010 \\ -0.062 & -1.094 & -0.147 \\ 0.139 & 1.299 & 1.626 \\ 0.188 & 0.268 & 0.074 \end{bmatrix} \begin{matrix} sp_1 \\ sp_2 \\ rm \\ dr_1 \\ dr_2 \end{matrix} \tag{23}$$

We can reduce these five equations to three by combining the second-order modes into the form of equation (14). We do this by dropping the sp_1 and dr_1 rows from the $\mathbf{T}^{-1}$ matrix and the sp_2 and dr_2 rows from the $\mathbf{S}$ matrix. Recall that equation (14) involves only y_{p+1} and w_p, so we drop y_p and w_{p+1} from consideration. Using the expressions for k and a from equations (13) and displayed in the $\mathbf{\Gamma}$ matrix above, we get

$$\begin{aligned} \ddot{y}_{sp_2} + 2.167\ \dot{y}_{sp_2} + 8.030\ y_{sp_2} &= w_{sp_1} \\ \dot{y}_{rm} + 2.750\ y_{rm} &= w_{rm} \\ \ddot{y}_{dr_2} + 0.973\ \dot{y}_{dr_2} + 10.135\ y_{dr_2} &= w_{dr_1} \end{aligned} \tag{24}$$

where (and now dropping the 1 and 2 subscripts from equations (24))

$$\begin{bmatrix} w_{sp} \\ w_{rm} \\ w_{dr} \end{bmatrix} = \underbrace{\begin{bmatrix} -1.234 & -1.762 & -0.347 \\ -0.062 & -1.094 & -0.147 \\ 0.139 & 1.299 & 1.626 \end{bmatrix}}_{\mathbf{S}} \begin{bmatrix} \delta e_L \\ \delta e_R \\ \delta r \end{bmatrix} \tag{25}$$

and the reduced $\mathbf{T}^{-1}$ matrix (used to obtain y_{sp}, y_{rm}, and y_{dr} from $\mathbf{x}$) is

$$\mathbf{T}^{-1} = \begin{bmatrix} 0.043 & 9.150 & 0.085 & -0.003 & -0.116 & -0.240 & -4.882 & 0.019 \\ 3.012 & -7.568 & -0.228 & -0.003 & 1.231 & 4.780 & 12.580 & -0.177 \\ -1.344 & -4.273 & 0.081 & 0.002 & -0.004 & -0.649 & 15.628 & -0.015 \end{bmatrix} \tag{26}$$

We will ultimately want to obtain $\mathbf{u}$ given $\mathbf{w}$, so we need to invert $\mathbf{S}$ from equation (25) to obtain $\mathbf{S}^{-1}$. $\mathbf{S}^{-1}$ is shown numerically below.

$$\begin{bmatrix} \delta e_L \\ \delta e_R \\ \delta r \end{bmatrix} = \underbrace{\begin{bmatrix} -0.885 & 1.346 & -0.068 \\ 0.045 & -1.092 & -0.089 \\ 0.040 & 0.757 & 0.692 \end{bmatrix}}_{\mathbf{S}^{-1}} \begin{bmatrix} w_{sp} \\ w_{rm} \\ w_{dr} \end{bmatrix} \tag{27}$$

Equations (24) are decoupled ordinary differential equations in the sense that the modal coordinates (y's) are not dependent on each other. The modal controls (w's), on the other hand, are linear combinations of the three natural controls (see eq. (25)), but because the number of modal controls is the same as the number of natural controls ($\mathbf{S}$ is a square matrix), the modal controls can be specified arbitrarily and independently through $\mathbf{S}^{-1}$, where $\mathbf{S}^{-1}$ is the inversion of the matrix in equation (25). This means that SISO control techniques can be used *independently* on each of the three equations (24). For example, with appropriate feedback, we can specify the closed-loop response of the short-period mode independent of what the roll mode and the Dutch roll mode characteristics are. Also note that if our controller for the short-period mode introduces additional eigenvalues to the overall system, the corresponding eigenvectors will be associated with the short-period mode and the time response of these new eigenvectors will remain decoupled from the other two fast modes.

We are not completely free to choose the time response independently for each mode in the case of the OWRA because the modes (or eigenvectors) are not satisfactory responses to direct pilot inputs. For instance, suppose we allowed longitudinal stick to be a direct command of the short-period mode. The response to aft stick would be a mild pitch up and a violent roll to the right. This would clearly be unsatisfactory. We need to take a linear combination of the three modes to produce a more satisfactory response to aft stick, say pitch up without the roll. This means that the effective closed-loop time constants for the three modes should all be approximately the same so that in combination the three responses will die out more or less together.

Choosing similar closed-loop response times should not be a problem, in any event, because the open-loop time responses should be similar in the first place. If they are not we can simply use cascaded outer loops to control the slower modes and avoid the coupling problem altogether.

It should also be pointed out that if the modes (or eigenvectors) are acceptable responses, as they are for a conventional airplane, then the closed-loop time constants for each mode can be quite different if desired.

The next thing we need to do is choose a SISO control technique for the three modes. We need one which has zero steady state error since our dynamic system is nonlinear. One obvious choice

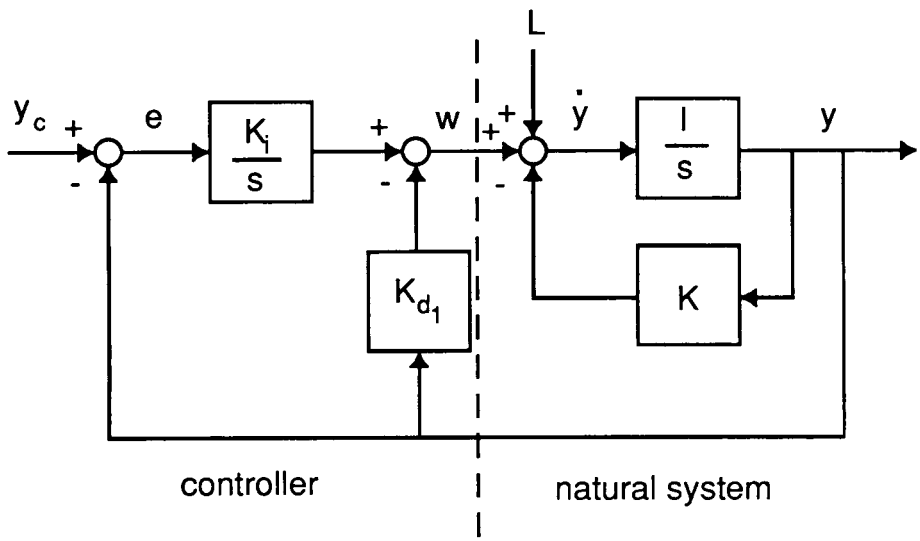

Figure 3. – Pseudo-derivative feedback of a first-order system.

is classical proportional plus integral (P+I) control and, in fact, this is part of the loop-shaping technique to be used on the actual OWRA. Phelan's pseudo-derivative feedback (PDF) technique (ref. 8) has many advantages over P+I control, but has no obvious MIMO implementation. PDF has much better load rejection for the same control power and more efficient dynamic response while retaining the zero steady state error behavior of P+I control. I chose to use PDF on the OWRA as an example of a SISO technique with definite advantages for nonlinear systems which could not until now be applied to a highly coupled MIMO system.

To use PDF on the OWRA, we will need algorithms for first- and second-order modes. In fact these two algorithms are all we will need for systems of arbitrary order, assuming nonrepeated roots of the characteristic equation, because we can always break the system into first- and second-order modes.

A block diagram of PDF applied to a first-order natural system, such as the roll mode, is shown in figure 3. The complete system is divided into the natural system (or open-loop system) and the controller. The combination of controller and natural system will also be called the closed-loop system. The operational equation for this system is

$$[s^2 + (k_{d_1} + k)s + k_i]\, y = k_i\, y_c + s\, L \tag{28}$$

By having a single integrator in the controller forward loop, PDF avoids introducing a zero into the command response transfer function. The result is a smoother response to commanded inputs and zero steady state error. However, the order of the closed-loop system is increased by one because of the controller integrator and the closed-loop system is second order.

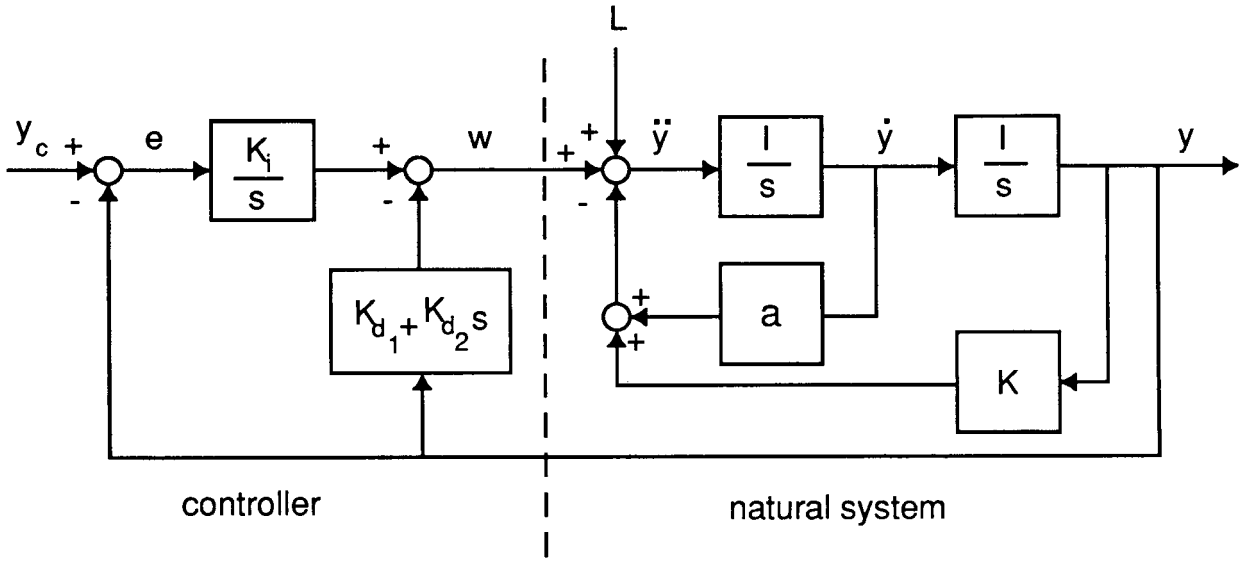

Figure 4. – Pseudo-derivative feedback of a second-order system.

The second-order response of this system can be set by the two controller gains: k_i and k_{d_1}. If we write the *desired* characteristic equation in terms of a desired damping ratio, ζ, and a desired time constant of the response envelope, $\tau = 1/(\zeta\omega_n)$, we get

$$s^2 + 2/\tau\, s + 1/(\tau^2\zeta^2) = 0 \tag{29}$$

Equating coefficients between equations (28) and (29), we can derive the controller gains in terms of the desired damping ratio, desired time constant, and the natural spring constant, k.

$$\begin{aligned} k_{d_1} &= 2/\tau - k \\ k_i &= 1/(\tau^2\zeta^2) \end{aligned} \tag{30}$$

The block diagram for PDF control of a second-order natural system is shown in figure 4. The controller is similar to that for a first-order system except that the derivative of the controlled variable is also required.

The operational equation for the closed-loop system is

$$[s^3 + (k_{d_2} + a)s^2 + (k_{d_1} + k)s + k_i]\; y = k_i\, y_c + s\, L \tag{31}$$

The closed-loop system is again one order greater than the open-loop system, i.e., third-order, and, in general, will have a second-order part and a real part. The third-order response of this system can be set by the three controller gains: k_i, k_{d_1}, and k_{d_2}. If we make the additional assumption that the time constant of the real part response is equal to the time constant of the second-order part's response envelope, then we can write a desired characteristic equation in terms of a desired damping ratio, ζ, and a desired time constant, $\tau = 1/(\zeta\omega_n)$.

$$(s + 1/\tau)(s^2 + 2/\tau\, s + 1/(\tau^2\zeta^2)) = 0 \tag{32}$$

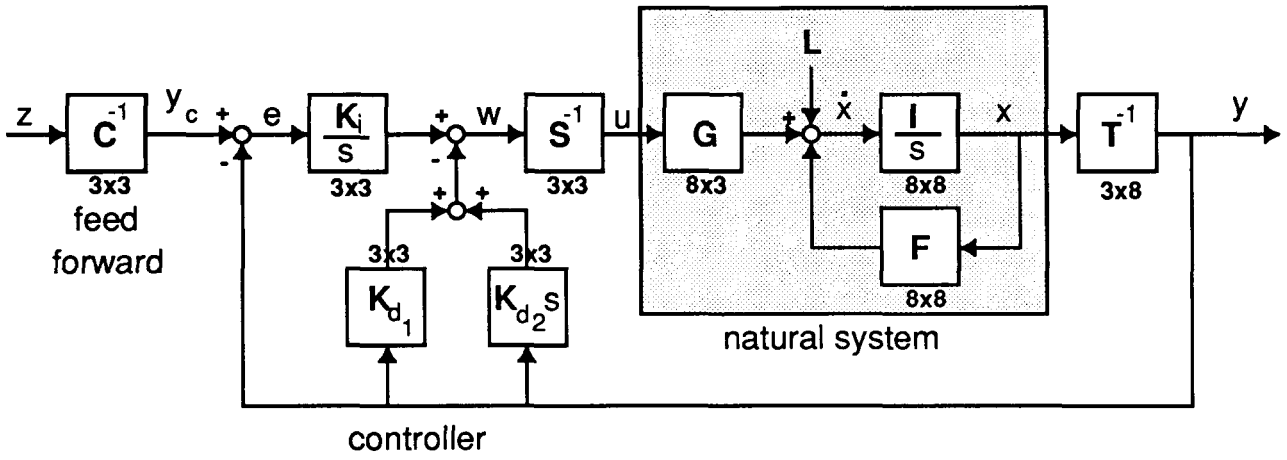

Figure 5. – Modal control system for the OWRA.

Equating coefficients between equations (31) and (32), we can derive the controller gains in terms of the desired damping ratio, the desired time constant, the natural spring constant, k, and the natural damping, a.

$$\begin{aligned} k_{d_2} &= 3/\tau - a \\ k_{d_1} &= (2 + 1/\zeta^2)/\tau^2 - k \\ k_i &= 1/(\tau^3 \zeta^2) \end{aligned} \tag{33}$$

The complete OWRA controller has only eight gains which affect the time response of the closed-loop system: two for the roll mode (eqs. (30)) and three each for the short-period and Dutch roll modes (eqs. (33)).

We now have the means to design a control system based on the reduced-order model of the system described by equations (24). We also have the transformation matrix from the natural state to the reduced modal coordinates ($\mathbf{y} = \mathbf{T}^{-1}\ \mathbf{x}$) given by equation (26) and the transformation matrix from the reduced modal controls to the natural controls ($\mathbf{w} = \mathbf{S}^{-1}\ \mathbf{u}$) given by equation (27). We will now apply this controller design to the full 8×8 system, equations (1), where $\mathbf{F}$ and $\mathbf{G}$ are given numerically in appendix B. The complete system can be put in matrix form as shown in figure 5.

The diagram shows that the $\mathbf{S}^{-1}$ and $\mathbf{T}^{-1}$ matrices are used to transform the full natural system into the assumed reduced modal system (eqs. (24)) between $\mathbf{w}$ and $\mathbf{y}$. Note that $\mathbf{T}^{-1}$ has only three rows and that $\mathbf{S}^{-1}$ is a square 3×3 matrix as we expect from the earlier discussion.

The control-gain matrices, $\mathbf{K}_i$, $\mathbf{K}_{d_1}$, and $\mathbf{K}_{d_2}$, are all 3×3 *diagonal* matrices because they represent independent SISO controllers for each mode. Note that all the coefficients corresponding to the roll mode are calculated using equations (30) and naturally the component of $\mathbf{K}_{d_2}$ corresponding to the roll mode is zero. All the other controller coefficients are calculated using equations (33).

Design time constants and damping coefficients for the OWRA were chosen consistent with the handling qualities specifications (ref. 7). This requires some explanation because the handling qualities specifications are written in terms of the open-loop eigenvalues, but the closed-loop response using PDF is one order larger for each mode, introducing extra eigenvalues. Specifically, for first-order natural modes the handling qualities specifications restrict the first-order time constant, but the response is second order, whereas for second-order natural modes the handling qualities specifications restrict the natural frequency and damping ratio, but the closed-loop response is third order. In the case of first-order natural modes, this inconsistency was resolved by setting the closed-loop damping ratio to one so the response appears first order. In the case of second-order modes, the inconsistency in order was resolved by setting the time constant corresponding to the real root equal to the time constant of the second-order part's response envelope so the response appears second order. The actual chosen values for the OWRA are shown below.

$$\begin{aligned} \zeta_{sp} &= 0.707 \ , \quad \tau_{sp} = 0.40 \\ \zeta_{rm} &= 1.000 \ , \quad \tau_{rm} = 0.13 \\ \zeta_{dr} &= 0.707 \ , \quad \tau_{dr} = 0.40 \end{aligned} \tag{34}$$

Applying equations (30) and (33) with these values and using the k and a values calculated from equations (13) and displayed along the diagonal of $\mathbf{\Gamma}$ in equations (23), the following control gains are obtained.

$$\begin{aligned} k_{i_{sp}} &= 31.25 \ , \quad k_{d_{1\,sp}} = 16.97 \ , \quad k_{d_{2\,sp}} = 5.33 \\ k_{i_{rm}} &= 59.17 \ , \quad k_{d_{1\,rm}} = 12.63 \ , \quad k_{d_{2\,rm}} = 0.00 \\ k_{i_{dr}} &= 31.25 \ , \quad k_{d_{1\,dr}} = 14.87 \ , \quad k_{d_{2\,dr}} = 6.53 \end{aligned} \tag{35}$$

The only matrix yet to be explained or evaluated is the feed-forward matrix, $\mathbf{C}^{-1}$. $\mathbf{C}^{-1}$ is a mixing matrix which takes the pilot command vector, $\mathbf{z}$ and produces the mode commands, $\mathbf{y}_c$. The vector, $\mathbf{z}$, was chosen by picking three components from the natural state vector, $\mathbf{x}$, which come to an approximately steady value in response to isolated step inputs in each mode and which might make sense to a pilot flying a symmetric airplane. The components chosen were

$$\mathbf{z} = [\alpha_c, \ p_c, \ \beta_c]^T \tag{36}$$

We will obtain $\mathbf{C}^{-1}$ by first obtaining $\mathbf{C}$ and then inverting it. The $\mathbf{C}$ matrix is the steady state transfer function from $\mathbf{y}_c$ to $\mathbf{z}$ (which, in this case, is a subset of $\mathbf{x}$). We can find $\mathbf{C}$ by simulation using the figure 5 block diagram to the right of the $\mathbf{C}^{-1}$ matrix where all the matrices have been identified. We put step inputs in at $\mathbf{y}_c$ and observe the steady response in $\mathbf{x}$ (which contains $\mathbf{z}$). For example, the first column of $\mathbf{C}$ is obtained by inputting a step in y_{sp_c} (y_{rm_c} and y_{dr_c} are zero) and observing the steady state change in the α, p, and β components of $\mathbf{x}$. This process is repeated with isolated step inputs to the roll and Dutch roll modes. The $\mathbf{C}$ matrix obtained is shown below.

$$\begin{bmatrix} \alpha \\ p \\ \beta \end{bmatrix} = \underbrace{\begin{bmatrix} 4.00 & 0.344 & 0.976 \\ 4.333 & 17.778 & -13.171 \\ 1.300 & 0.000 & 2.049 \end{bmatrix}}_{\mathbf{C}} \begin{bmatrix} y_{sp_c} \\ y_{rm_c} \\ y_{dr_c} \end{bmatrix} \tag{37}$$

We can invert $\mathbf{C}$ to get $\mathbf{C}^{-1}$ as shown numerically below.

$$\begin{bmatrix} y_{sp_c} \\ y_{rm_c} \\ y_{dr_c} \end{bmatrix} = \underbrace{\begin{bmatrix} 0.319 & -0.006 & -0.192 \\ -0.228 & 0.061 & 0.498 \\ -0.202 & 0.004 & 0.610 \end{bmatrix}}_{\mathbf{C}^{-1}} \begin{bmatrix} \alpha_c \\ p_c \\ \beta_c \end{bmatrix} \tag{38}$$

It is important that the components of the $\mathbf{z}$ vector have approximately steady responses to step inputs in each mode. This ensures that linear combinations of the mode commands (from $\mathbf{C}^{-1}\,\mathbf{z}$) will result in steady time responses. Steady and nonsteady responses to different mode commands cannot be added or mixed in any useful way.

At this point, we have obtained all the matrices in figure 5. The question now arises as to whether the assumptions which allowed the original eight-equation set to be reduced to three and upon which the controller design is based are valid. A linear analysis of the system shown in figure 5 with the full 8×8 natural system imbedded was performed to see if the closed-loop roots are indeed moved to the desired location.

To investigate the eigenvalues and eigenvectors of the closed-loop system in figure 5, we need the system equations with the control input, $\mathbf{y_c}$, and the load to the system, $\mathbf{L}$, set to zero. Three new auxiliary states are required to describe the system as a set of first-order equations because of the three integrators introduced by the controller ($\mathbf{K}_i/s$). The complete system is eleventh order. A natural choice for the three auxiliary states, χ, is the integral of the reduced modal state vector, $\mathbf{y}$. Mathematically,

$$\dot{\chi} = \mathbf{y} \tag{39}$$

Now we can write the controller as

$$\mathbf{w} = -\mathbf{K}_i\,\chi - \mathbf{K}_{d_1}\,\mathbf{y} - \mathbf{K}_{d_2}\,\dot{\mathbf{y}} \tag{40}$$

The $\mathbf{S}^{-1}$ and $\mathbf{T}^{-1}$ matrices are used to transform the natural system into the assumed reduced modal system as follows:

$$\begin{aligned} \mathbf{y} &= \mathbf{T}^{-1}\,\mathbf{x} \\ \mathbf{u} &= \mathbf{S}^{-1}\,\mathbf{w} \end{aligned} \tag{41}$$

Substituting equations (41) into equation (40), we can write the natural controls in terms of the natural states and the modal integral states.

$$\mathbf{u} = \mathbf{S}^{-1}[-\mathbf{K}_i\,\chi - \mathbf{K}_{d_1}\mathbf{T}^{-1}\,\mathbf{x} - \mathbf{K}_{d_2}\mathbf{T}^{-1}\,\dot{\mathbf{x}}] \tag{42}$$

To obtain the overall closed-loop equation, we substitute equation (42) into the natural-state equation, equation (1). The result is

$$\dot{\mathbf{x}} = \mathbf{F}\,\mathbf{x} + \mathbf{G}\mathbf{S}^{-1}[-\mathbf{K}_i\,\chi - \mathbf{K}_{d_1}\mathbf{T}^{-1}\,\mathbf{x} - \mathbf{K}_{d_2}\mathbf{T}^{-1}\,\dot{\mathbf{x}}] \tag{43}$$

Rewriting this in state-equation form, we obtain

$$[\mathbf{I} + \mathbf{G}\mathbf{S}^{-1}\mathbf{K}_{d_2}\mathbf{T}^{-1}]\,\dot{\mathbf{x}} = [\mathbf{F} - \mathbf{G}\mathbf{S}^{-1}\mathbf{K}_{d_1}\mathbf{T}^{-1}]\,\mathbf{x} - \mathbf{G}\mathbf{S}^{-1}\mathbf{K}_i\,\chi \tag{44}$$

Writing this in standard form, with the full eleven-state vector, we obtain

$$\begin{bmatrix} \dot{\mathbf{x}} \\ \dot{\chi} \end{bmatrix} = \begin{bmatrix} \mathbf{D}^{-1}\mathbf{N} & -\mathbf{D}^{-1}\mathbf{G}\mathbf{S}^{-1}\mathbf{K}_i \\ \mathbf{T}^{-1} & \mathbf{\Phi} \end{bmatrix} \begin{bmatrix} \mathbf{x} \\ \chi \end{bmatrix} \tag{45}$$

where $\mathbf{\Phi}$ is the null matrix and

$$\begin{aligned} \mathbf{N} &= \mathbf{F} - \mathbf{G}\mathbf{S}^{-1}\mathbf{K}_{d_1}\mathbf{T}^{-1} \\ \mathbf{D} &= \mathbf{I} + \mathbf{G}\mathbf{S}^{-1}\mathbf{K}_{d_2}\mathbf{T}^{-1} \end{aligned} \tag{46}$$

The eigenvalues of this system for the design condition are shown below in comparison to the desired values implied by the design damping ratios and time constants, i.e., equations (29) and (32).

$$\begin{aligned} \lambda_{sp} &= -2.448,\ -2.603 \pm 2.551j \approx -2.5,\ -2.5 \pm 2.5j \\ \lambda_{ph} &= -0.007 \pm 0.053j \approx 0,\ 0 \\ \lambda_{rm} &= -9.002,\ -6.409 \approx -7.692,\ -7.692 \\ \lambda_{spl} &= -0.030 \approx 0 \\ \lambda_{dr} &= -1.772,\ -2.210 \pm 2.588j \approx -2.5,\ -2.5 \pm 2.5j \end{aligned} \tag{47}$$

The eigenvalues are reasonably well placed, although not perfectly, and the slow modes (the phugoid and spiral), which were neglected in the controller design, have hardly been disturbed from their open-loop values, equations (19). All the eigenvalues are considerably improved in speed and damping over the open-loop values given earlier.

Even though the eigenvalues have been positioned suitably (frequency domain engineers will recognize this as pole placement), the question remains whether the eigenvectors are still decoupled as in equation (3). To test this aspect, open- and closed-loop time history responses to modal pulse inputs were performed for each mode. The results are shown in figures 6-11.

The open-loop response for each mode (figs. 6, 8, and 10) is the result of a pure pulse input to the desired mode, i.e., one component of the $\mathbf{w}$ vector in figure 5 is pulsed with the controller feedback path disconnected, and the time response of the $\mathbf{y}$ vector is observed. This is equivalent to exciting one of the equations of equations (24) and observing the response of the other two equations. There should be no response in these other two equations if the three equations are truly decoupled as written. Examining figures 6, 8, and 10, we see that in each case the response in the other two modes is at least an order of magnitude less than the excited mode, except for the short-period mode, which shows some coupling to the Dutch roll. All three modes show their open-loop damping and frequency. Note the characteristic low damping of the Dutch roll mode.

The closed-loop response for each mode (figs. 7, 9, and 11) is the result of a pulse input to the mode command with all loops closed and with the design dampings and frequencies, equations (34). This corresponds to pulsing one component of the $\mathbf{y}_c$ vector in figure 5 and observing the time response of the $\mathbf{y}$ vector. In each case the decoupling is even more evident than in the open-loop case and the response is smoother. In the case of the roll mode, the response is noticeably more rapid.

This demonstrates that the assumptions used in deriving equations (24) are valid for the OWRA system and that the equations remain decoupled even with independent feedback loops around each equation.

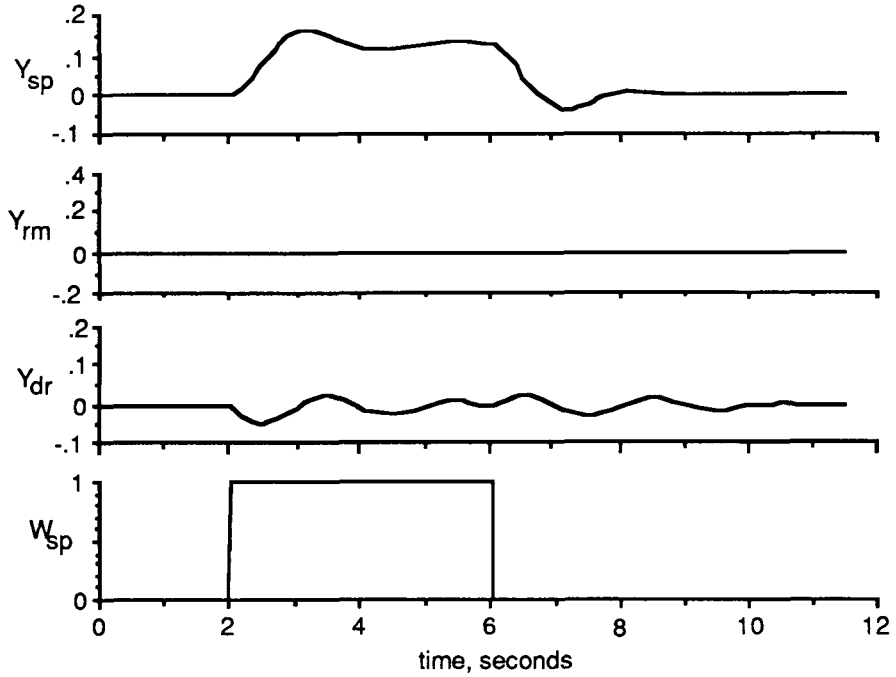

Figure 6. – Open-loop, short-period response.

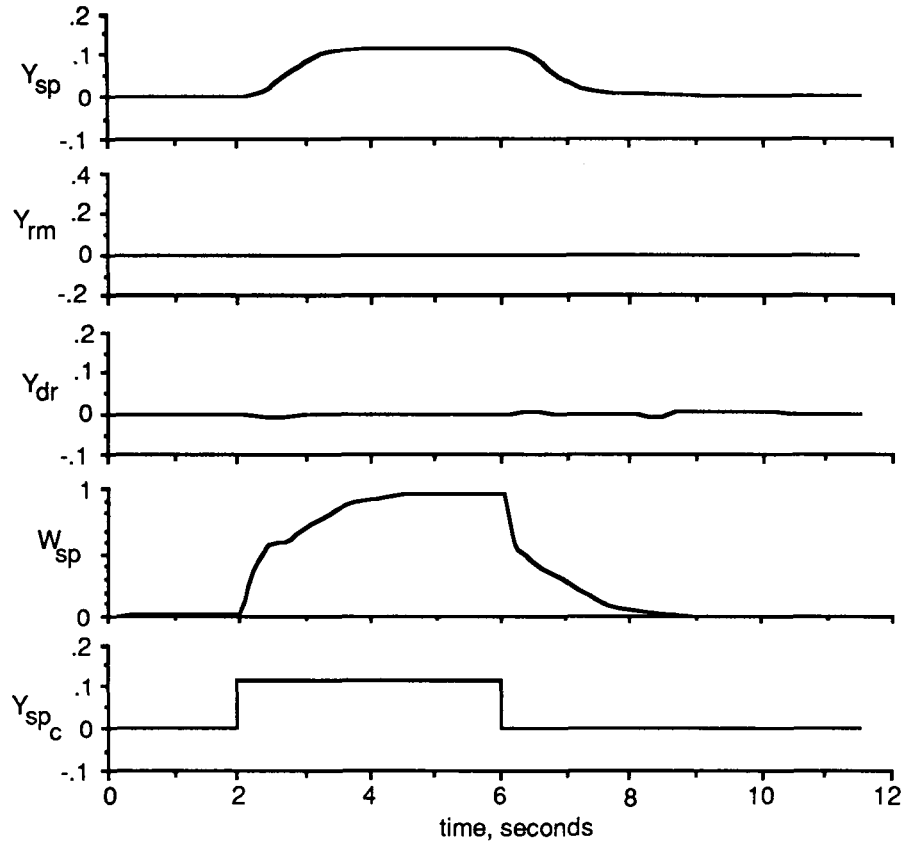

Figure 7. – Closed-loop, short-period response.

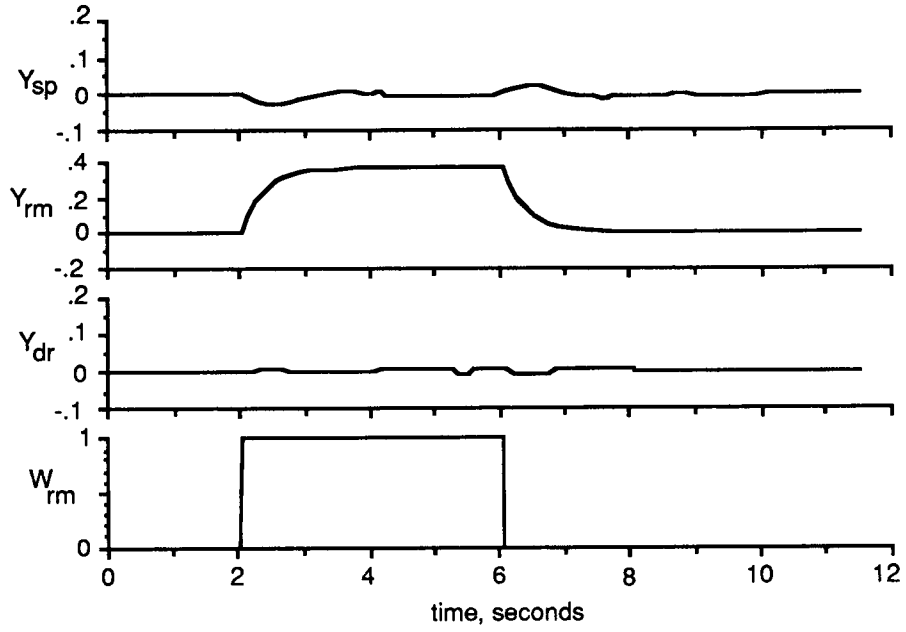

Figure 8. – Open-loop, roll-mode response.

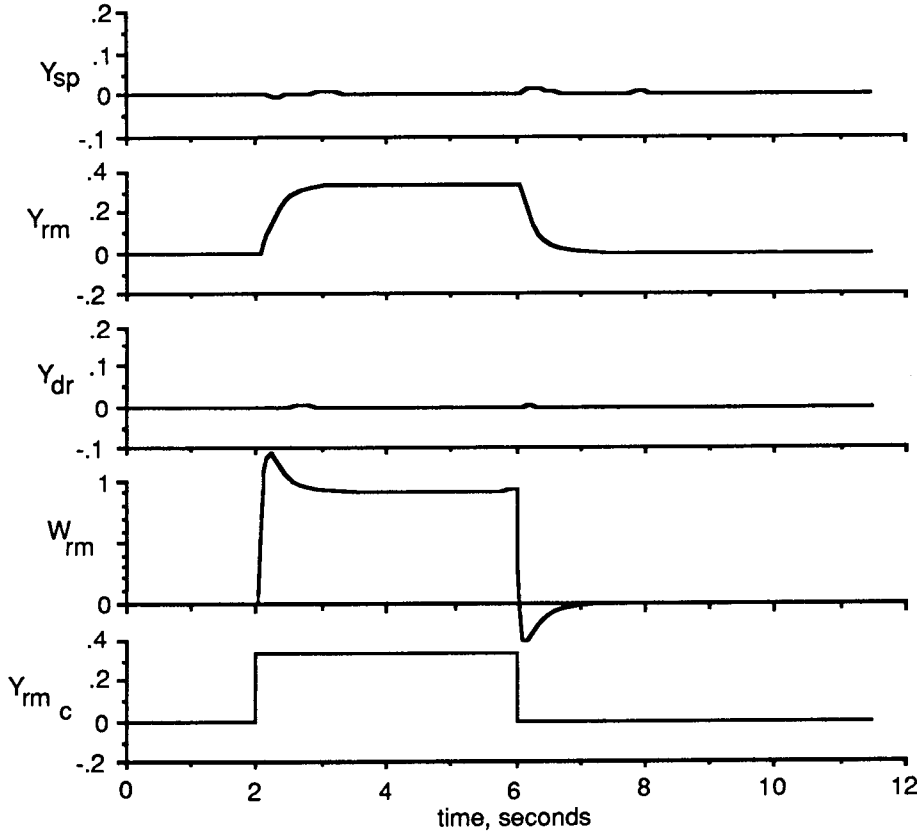

Figure 9. – Closed-loop, roll-mode response.

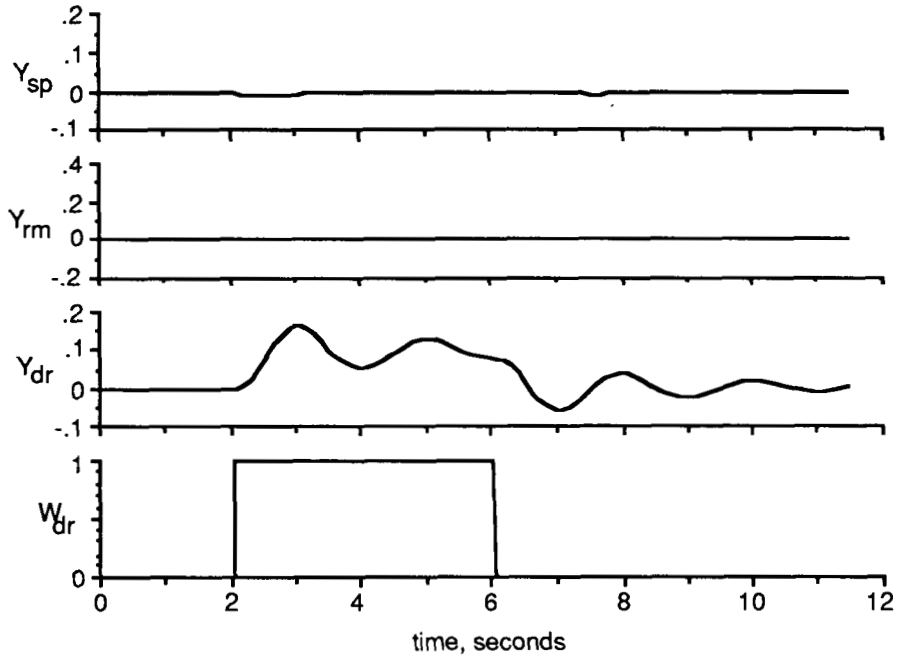

Figure 10. – Open-loop, Dutch roll response.

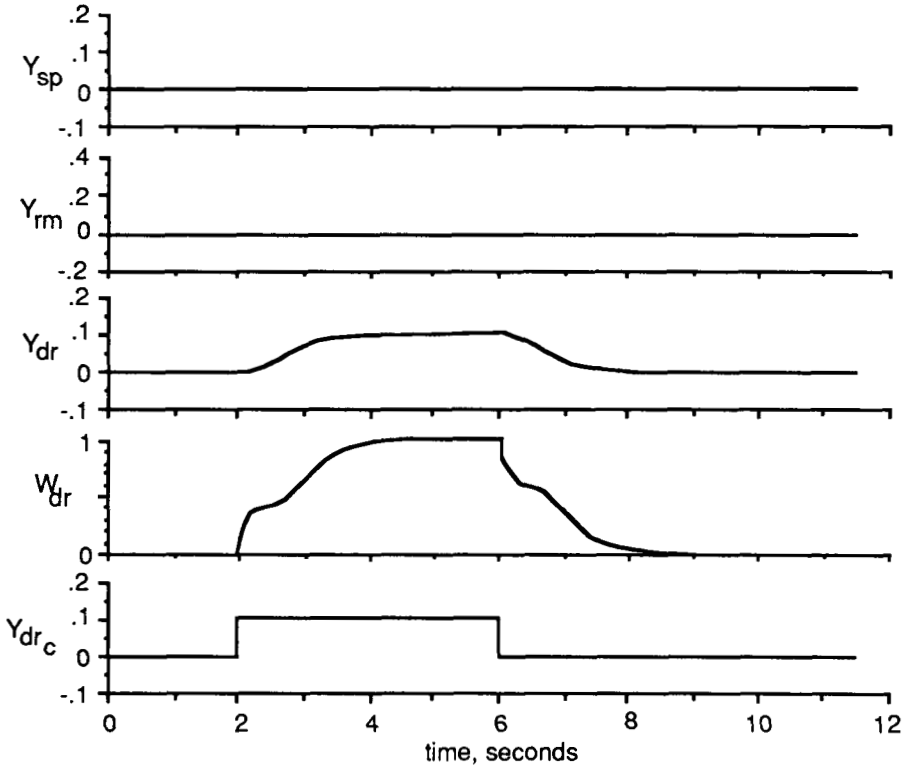

Figure 11. – Closed-loop, Dutch roll response.

NONLINEAR SIMULATION AND CONTROL LIMITING

Up to this point the OWRA has been modeled as a linear system (eq. (1)). Two unrealistic assumptions are implicit in this linear model. The first questionable assumption is that a control system designed with partial derivatives obtained at a single perturbation point will have identical response at any other point in the state space. The second questionable assumption is that the response is unbounded, that is, infinite control power is available. For most real aircraft both of these assumptions are invalid and the resulting control saturation or strong nonlinearities may cause a linear controller to go unstable. One possible solution is to limit the desired speed of response such that excursions into a nonlinear region do not happen too rapidly and such that the controller never commands the controls to be saturated. In the case of a highly nonlinear natural system (such as the OWRA) with external inputs of arbitrary magnitude, it becomes almost impossible to avoid having occasional saturation of the controls and still have reasonably rapid response. Because it is desired to apply the modal control algorithm to real oblique-wing aircraft (the OWRA, for example), it was felt that the closed-loop system should be dynamically stable with realistic inputs and disturbances large enough to cause saturation of the controls.

The following section describes additions to the linear modal control algorithm to realistically control the OWRA. It was found that nothing more than the added robustness of PDF control was needed to handle the nonlinearity of the OWRA. This is perhaps not surprising in view of the several linear control laws mentioned in the introduction which have successfully controlled the OWRA (refs. 2, 4, and 5). However, adequate decoupling of the longitudinal and lateral-directional aircraft response, which was a major goal, required an additional outer roll loop which will be described. The possibility of control saturation in both position and rate also required added new logic which will likewise be described.

In order to test the various other linear control laws discussed in the introduction, NASA has developed a detailed simulation of the OWRA (ref. 9). This simulation includes the full nonlinear equations of motion, the complete nonlinear aerodynamics with lookup tables from available wind tunnel and flight-test data, and control rate and position limits (significant nonlinearities). In the present investigation, this simulation was moved to another computer and run "off line" to demonstrate the new modal control law with a more realistic model.

After encouraging results from the linear model (figs. 6-11), the modal control law was applied to the nonlinear simulation. This corresponds to substituting the nonlinear OWRA simulation for the block labeled "natural system" in figure 5. Several basic dynamic checks were run with satisfactory responses, but the acid test for an oblique-wing aircraft is a pitch command because of the significant longitudinal-lateral coupling. From observations of pulse angle-of-attack commands (α_c from $\mathbf{z}$), it became apparent that the unwanted roll response was too large because although the steady-state roll rate is zero, the roll angle excursion during the pitch maneuver is excessive, and the steady-state roll angle may not be zero.

To reduce this excessive roll response, an outer-roll loop has been added which nulls roll-angle error. The roll-angle command is the time integral of lateral stick position, i.e., lateral stick commands roll rate. The response-time history to a pulse in angle-of-attack command is shown in

figure 12 with the roll loop open (solid lines) and closed (dashed lines). Note that angles are in degrees and angular rates are in degrees/second.

The solid lines in figure 12 (roll loop open) show that the complete control system from figure 5 (including the mixing matrix, $\mathbf{C}^{-1}$) successfully controls the nonlinear simulation of the OWRA, that is, a pulse in α has been commanded and obtained (curve 1 at 6 sec) with zero steady-state roll rate (curve 4 at 6 sec), but with $-2°$ of bank angle (curve 3 at 6 sec). The response is stable and can be modeled as a first-order system. Similar time histories (not shown) were generated for pulse roll rate and pulse sideslip inputs, respectively. These time histories show that the closed-loop response for each component of the pilot input vector, $\mathbf{z}$, is stable and can be modeled as a first-order system with the time constants selected in equations (34).

The closing of the roll loop (dashed lines in fig. 12) significantly reduces the roll excursion, as can be seen by examining the roll time history (curve 3 in fig. 12). The roll angle returns to zero during the angle-of-attack pulse with the roll loop closed (dashed line), whereas the roll angle comes to steady state at about $-2°$ with the roll loop open (solid line). Also note that the closing of the roll loop does not disturb the pitch response (compare the solid and dashed lines in curve 2, fig. 12).

The added roll loop block diagram is shown in figure 13. The roll loop is PDF control with the closed-loop roll-rate transfer function modeled as a first-order system with the time constant of the closed-loop roll mode. In figure 5 this transfer function exists between p_c, a component of the $\mathbf{z}$ vector, and p, a component of the $\mathbf{x}$ vector. The operational equation for the complete system as shown in figure 13 is

$$\left(s^3 + \frac{1}{\tau_{rm}} s^2 + \frac{k_{d_\phi}}{\tau_{rm}} s + \frac{k_{i_\phi}}{\tau_{rm}}\right) \phi = \frac{k_{i_\phi}}{\tau_{rm}} \left(\frac{k_r}{s} p_c\right) \tag{48}$$

which is third order. Recall that a desired third-order response (eq. (32)) has already been given in terms of a desired time constant and damping ratio. If we multiply out equation (32) and substitute the desired roll-loop time constant, τ_ϕ, and the desired roll-loop damping ratio, ζ_ϕ, we get

$$s^3 + 3/\tau_\phi\, s^2 + (2 + 1/\zeta_\phi^2)/\tau_\phi^2\, s + 1/(\tau_\phi^3 \zeta_\phi^2) = 0 \tag{49}$$

Comparing coefficients of the s^2 term in equations (48) and (49), we see that in order to preserve the form of equation (49) we have lost our freedom to choose τ_ϕ ($\tau_\phi = 3\tau_{rm}$). Then for a desired ζ_ϕ the control gains should be

$$\begin{aligned} k_{d_\phi} &= \left(\tfrac{1}{\zeta_\phi^2} + 2\right)/(9\ \tau_{rm}) \\ k_{i_\phi} &= 1/(27\ \tau_{rm}^2\ \zeta_\phi^2) \end{aligned} \tag{50}$$

The roll loop (fig. 13) is an example of a cascaded outer loop. Despite the relatively small ratio of time constants ($\tau_\phi = 3\tau_{rm}$), the roll angle is controlled without noticeably destabilizing other modes (fig. 12).

For the small input used to generate figure 12, the controls do not saturate and the response is comparable to that of the linear model. For larger inputs, the nonlinear aerodynamic behavior and

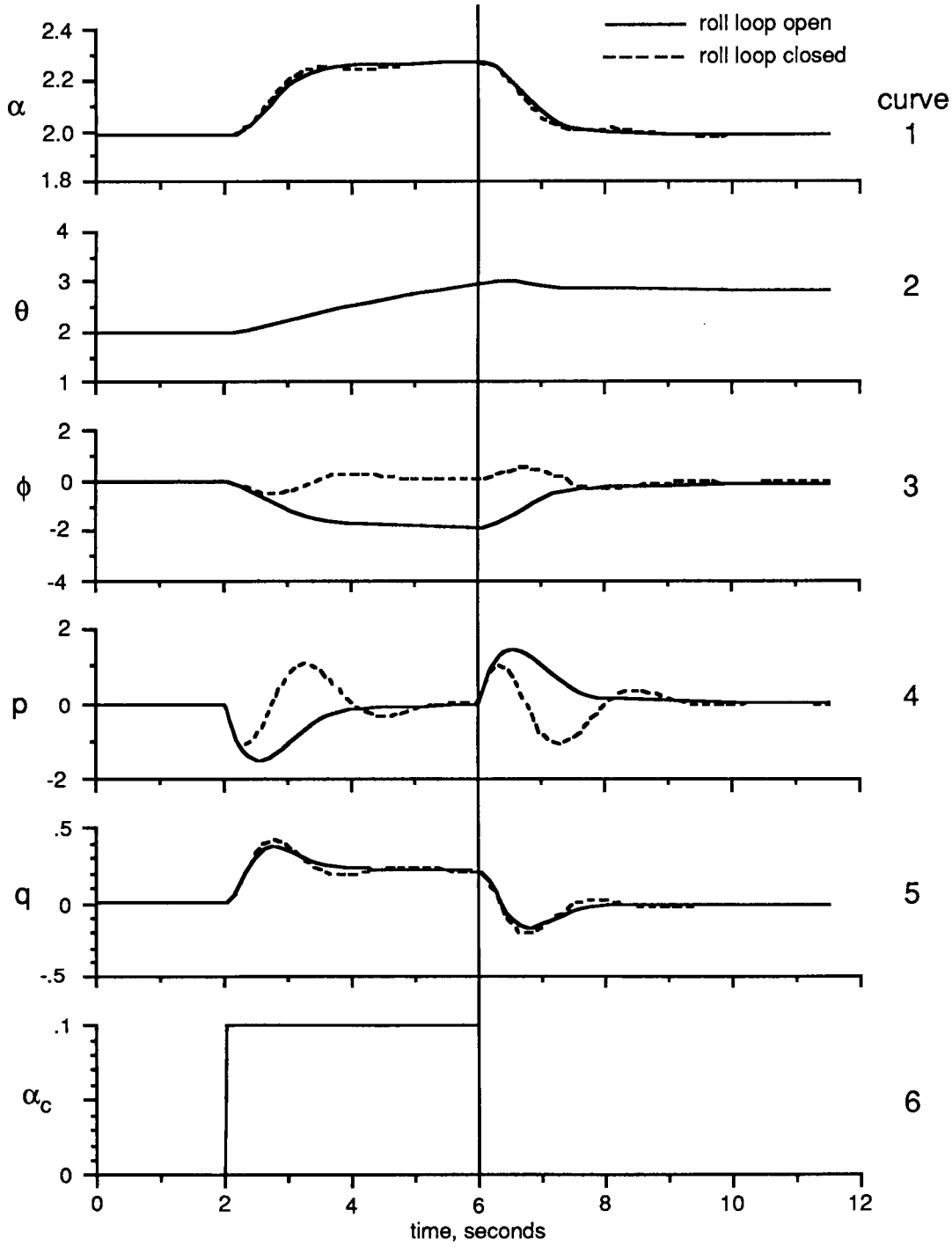

Figure 12. – Roll outer-loop comparison.

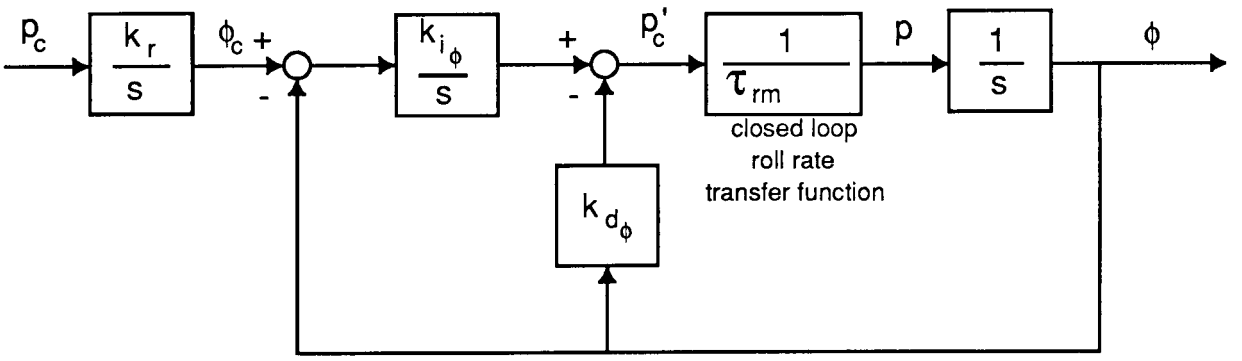

Figure 13. – Pseudo-derivative feedback control of the roll angle.

control saturation cause the linear control system designed this far to go unstable. The basic cause is the well-known "integrator windup" where the control system integrators build up too great an integrated error signal during saturation and end up, at best, overcontrolling the system and, at worst, driving the controls from one extreme to the other. The problem is compounded by the fact that the controls are applied in combination, yet each one can saturate independently in rate and/or position.

The best solution I found to this problem was to restrict the pilot input vector, $\mathbf{z}$, in figure 5, such that the controller never causes any control (a component of $\mathbf{u}$ in fig. 5), to saturate. For minimum response time, however, the restricted pilot input vector should be *as large as possible* in the intended direction without causing the controls to saturate. In other words, the restricted pilot input is such that at least one control is on the verge of saturation. If this is done, the controller never actually enters nonlinear operation, but the maximum possible control power is applied in the vector direction the pilot intended.

For example, suppose initially the OWRA is in trim with pilot input vector, $\mathbf{z}_0$, for which the controller output is the vector $\mathbf{u}_0$ (fig. 5). A short time later, the pilot introduces a new large input, $\mathbf{z}_1$, for which the unrestricted controller output is $\mathbf{u}_1$ and several components of $\mathbf{u}_1$ are saturated, or outside the known physical limits of that component. Now the vector difference $\Delta\mathbf{z} = \mathbf{z}_1 - \mathbf{z}_0$ defines a direction and magnitude for the pilot's desired *change* in state. If the direction is preserved, but the magnitude is allowed to vary from zero to $|\Delta\mathbf{z}|$, there will be some intermediate input, $\mathbf{z}_1' = \mathbf{z}_0 + \Delta\mathbf{z}'$, where $0 \leq \Delta\mathbf{z}' < \Delta\mathbf{z}$, for which the controller output is $\mathbf{u}_1'$ and at least one control (a component of $\mathbf{u}_1'$) is almost, but not quite, saturated. $\mathbf{z}_1'$ is taken as the new restricted controller input and the new control positions will be $\mathbf{u}_1'$.

If the controller is implemented digitally, iterative techniques can be used to determine $\Delta\mathbf{z}'$ to any desired accuracy, limited only by available computational power and the time between steps. It was found that the most reliable way to do this is to perform a binary search between the old command, $\mathbf{z}_0$, and the unrestricted new command, $\mathbf{z}_1$. For example, consider figure 14, which shows a schematic of the binary search with a limit of four iterations.

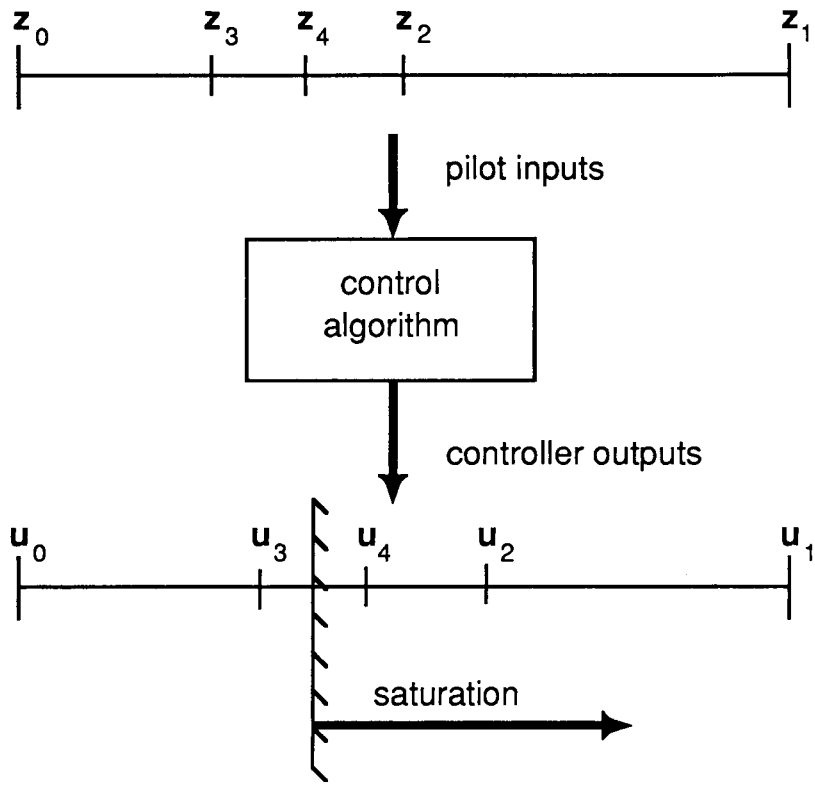

Figure 14. – Binary search for control saturation.

Figure 14 shows that for each possible input, $\mathbf{z}_i$, there is a corresponding output from the controller, $\mathbf{u}_i$, which may or may not be saturated. Note that if any component of the vector $\mathbf{u}_i$ is saturated, then $\mathbf{u}_i$ is considered to be saturated. At the start of the iteration, it is known that $\mathbf{u}_0$ is not saturated and $\mathbf{u}_1$ is saturated. At each intermediate step in the search, the new $\mathbf{z}_i$ is chosen as halfway between the smallest known $\mathbf{z}_i$ which causes saturation and the largest known $\mathbf{z}_i$ which does not cause saturation, i.e., the bounding inputs. For example, $\mathbf{z}_3$ is chosen halfway between $\mathbf{z}_0$ and $\mathbf{z}_2$ because, of the three known inputs, $\mathbf{z}_2$ is the smallest which causes saturation ($\mathbf{u}_2$ is saturated) and $\mathbf{z}_0$ is the largest which does not cause saturation ($\mathbf{u}_0$ is not saturated). At the end of the search, the largest known input which does not cause saturation is chosen as the restricted input, in this case $\mathbf{z}_3$. The corresponding control, $\mathbf{u}_3$, is the restricted output of the controller. This ensures that the controller never sees an input which will ultimately saturate a control.

The advantages of this binary search are that a known and consistent accuracy ($|\Delta \mathbf{z}|/2^{n-1}$) is obtained after a fixed number of cycles and that the result of the search will never saturate a control. One disadvantage is that additional cycles through the control code are required during saturation. Also, this algorithm assumes that there is one and only one boundary of saturation in the mapping of $\mathbf{z}$ to $\mathbf{u}$.

The algorithm described thus far works well if saturation results from a large pilot input, but does not address the situation where a large error signal is caused by an external disturbance, for

example, an atmospheric gust. In the case of an external disturbance (**L** in fig. 5), the resulting large error signal (**e** in fig. 5) may cause control saturation without a change in pilot input. There are now two possible unusable situations: (1) the pilot input from the previous time step may now lead to saturation with the effect of the disturbance (recall that in fig. 14 we assumed that $\mathbf{u}_0$ was unsaturated) and (2) the desired vector control direction, $\Delta\mathbf{z}$, may be undefined, that is, if no new pilot input is supplied, then $\mathbf{z}_0 = \mathbf{z}_1$ in figure 14.

This problem and its solution are more easily explained in terms of a simple, one-dimensional example which nevertheless contains all the important control saturation features of the modal controller applied to the OWRA (fig. 5). Consider the zeroth-order natural system with proportional feedback diagrammed at the top of figure 15. The symbols chosen are loosely based upon a longitudinal control system for an aircraft where α is the angle of attack, α_c is the pilot input and desired angle of attack, α_g is atmospheric turbulence, e is the error signal, and δ is a control surface which has physical position limits.

The closed-loop operational equation listed below the diagram indicates that to both reduce the gust response and improve the input to output response, the gain, k, should be relatively large. However, the formula for control position, δ, shows that saturation can be caused by pilot input, α_c, or by a gust, α_g, and that a relatively large gain will cause saturation for relatively small pilot inputs and/or gusts. As control engineers, we can choose to limit the size of pilot inputs and we can choose a small gain and therefore slow the response in order to avoid saturation of the control. However, we can do nothing about the size of gusts.

The worst case, then, is a large gust capable of causing saturation without additional pilot input. We can't apply the previous input restriction algorithm because we don't have a pair of distinct pilot inputs, one that causes saturation and one that does not, between which we can perform the binary search. A modified approach is illustrated in figure 15.

Below the block diagram in figure 15 are possible time histories of control system variables for different possible control inputs in the presence of a large gust. The thin solid line represents the system response with no modification to the pilot input. At time 0, the system is undisturbed. At time 1, a large positive gust has appeared, causing a large negative error ($e = \alpha_c - \alpha_g$), which then causes an excessive control command ($\delta = k\ e$) which exceeds the control limit represented by a hashed line. We can now ask what *artificial* pilot input applied simultaneously with the gust would result in no change in the control, δ, from time 0 to time 1. This case is represented by the dashed lines in figure 15. At time 1, a large positive pilot input matches the large positive gust, resulting in zero error, which causes no change in the control. In other words, to keep the control from moving, the pilot should command the gust response. Somewhere in between doing nothing (the thin solid line) and commanding the gust (the dashed line) is a pilot input which helps to mitigate the effect of the gust, but which results in a control position just within the physical limits of the control (the hashed line). This is the best pilot input within the limits of the available control power.

The analogy between the input restriction algorithm for large pilot inputs (previously described) and the best pilot input algorithm for gusts illustrated in figure 15 is as follows. In each case there are two known pilot inputs, one that causes saturation and one that does not. A binary search is performed between the two for an intermediate input which moves the controls in a "desired"

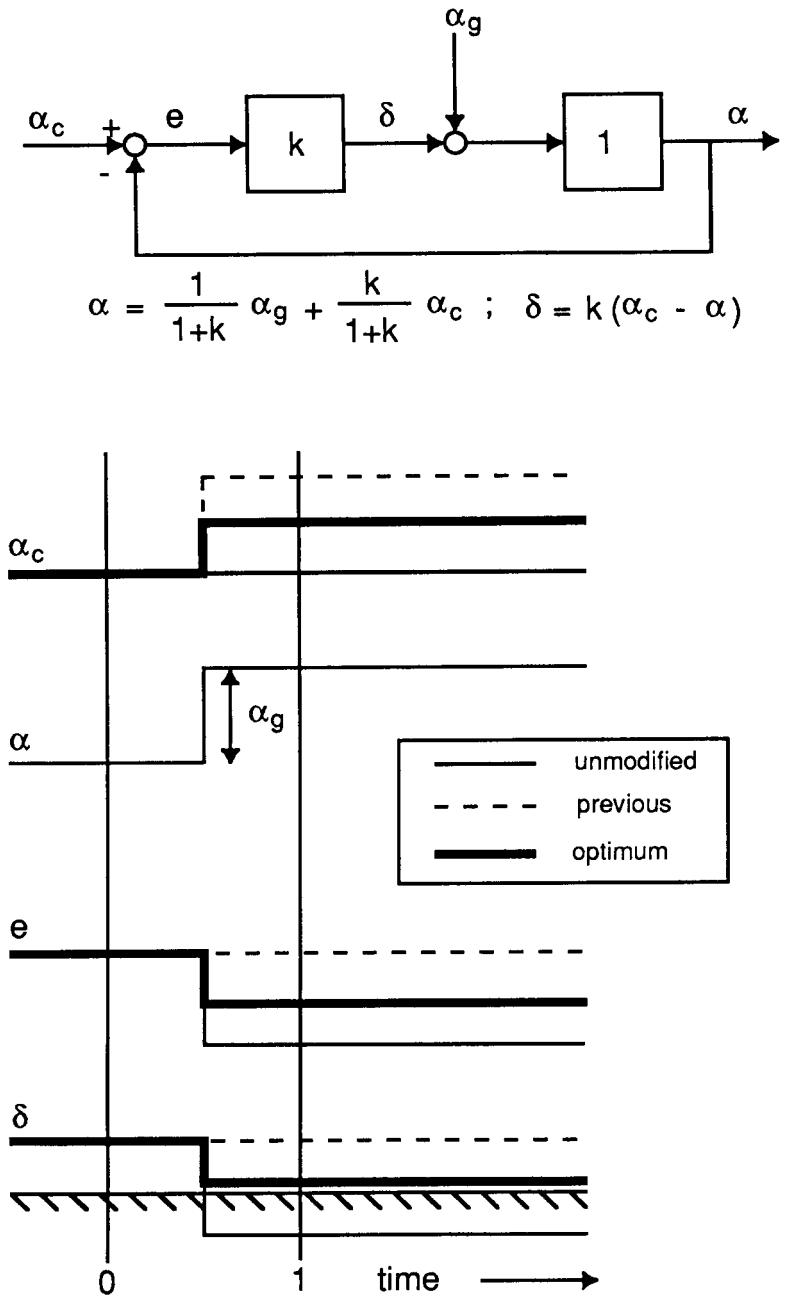

Figure 15. – Control saturation caused by an external disturbance.

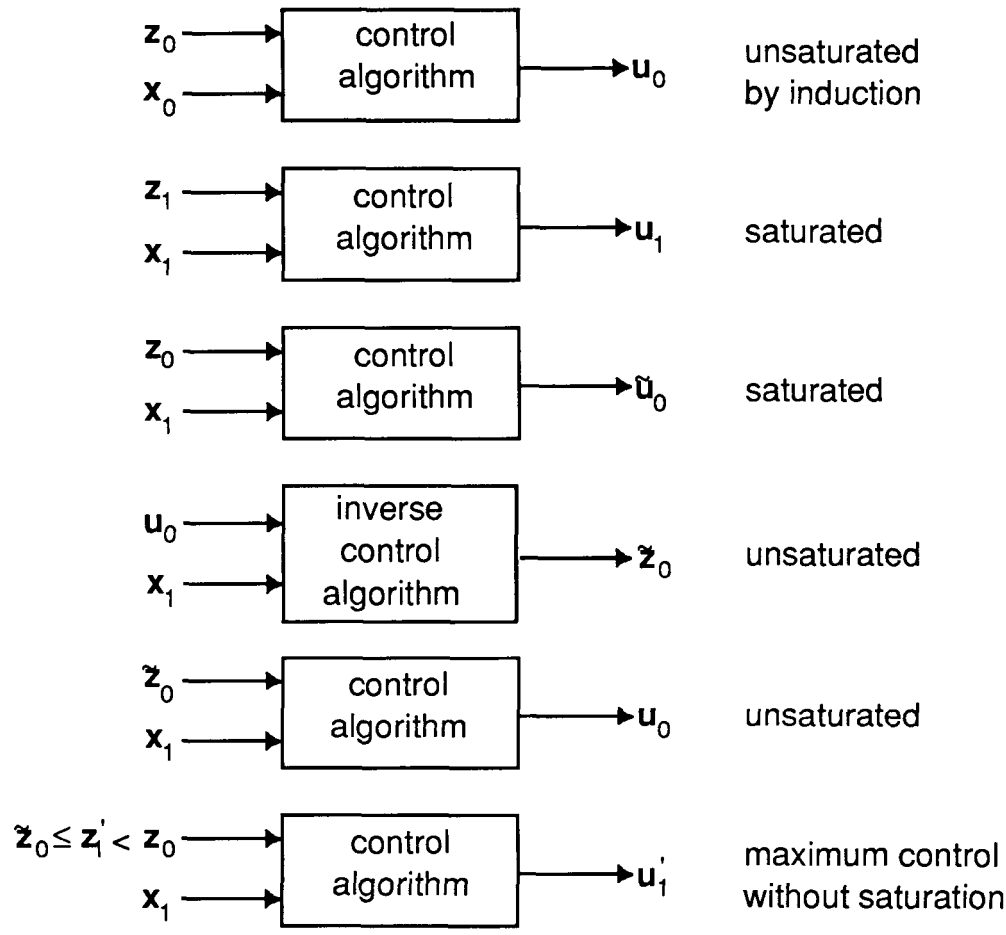

Figure 16. – Input limiting with external disturbances.

direction, but does not quite saturate any control. When saturation is caused by pilot input, the desired direction is from the old input toward the new input. When saturation is caused by external disturbance, the desired direction is from an artificial input which commands the disturbance (but results in no change in the control positions) toward the old input, which attempts to maintain equilibrium in the presence of the gust (but results in saturation of the controls).

Figure 16 illustrates how these ideas can be applied to the OWRA. This figure shows the sequence of steps for handling control saturation of the system in figure 5. Referring to figure 5, the controller is defined as everything external to the shaded box labeled the natural system. The controller takes as input the state vector, $\mathbf{x}$, and the pilot input vector, $\mathbf{z}$, and outputs the new control vector, $\mathbf{u}$.

Now referring to figure 16, at the old time step (before the gust), the controller takes as input $\mathbf{z}_0$ and $\mathbf{x}_0$ and outputs $\mathbf{u}_0$, which is unsaturated (line 1). It is unsaturated because the algorithm I am about to describe always produces an unsaturated result (an example of mathematical induction).

At the new step (line 2), the controller takes as input the new state, $\mathbf{x}_1$, and the new pilot input, $\mathbf{z}_1$, and produces the new unmodified controls, $\mathbf{u}_1$. If $\mathbf{u}_1$ is not saturated, the controller is done, i.e., lines 1 and 2 represent the normal unsaturated sequence.

If $\mathbf{u}_1$ is saturated, as indicated, the next step (line 3) is to determine whether saturation is caused by pilot input or by external disturbance. The controller takes as input the old pilot input, $\mathbf{z}_0$, and the new state, $\mathbf{x}_1$, to produce a modified "old" control vector, $\tilde{\mathbf{u}}_0$. If $\tilde{\mathbf{u}}_0$ is unsaturated, then the new pilot input is the cause of saturation and a binary search is performed between lines 2 and 3. The restricted controller input will be somewhere between $\mathbf{z}_0$ and $\mathbf{z}_1$ and the controller output will be somewhere between $\tilde{\mathbf{u}}_0$ and $\mathbf{u}_1$.

However, if $\tilde{\mathbf{u}}_0$ is saturated, as indicated, then an external disturbance is the cause and the next step is to find the artificial pilot input, $\tilde{\mathbf{z}}_0$, which commands the disturbance in the new state, $\mathbf{x}_1$, and produces no change in the controls from the previous time step (analogous to the dashed lines in fig. 15). This desired relationship is shown in line 5 of figure 16.

$\tilde{\mathbf{z}}_0$ can be calculated directly by going exactly backwards through the controller algorithm, in effect using $\mathbf{u}_0$ and $\mathbf{x}_1$ as input to an "inverse" of the controller, as shown in line 4 of figure 16. Referring to figure 5, the inverse controller is obtained as follows. We can multiply $\mathbf{u}_0$ by $\mathbf{S}$ (eq. (25)) to obtain $\tilde{\mathbf{w}}$. Now we already know $\mathbf{y}_1$ and $\dot{\mathbf{y}}_1$ from a previous calculation (line 2 of fig. 16), so we can *add* $\mathbf{K}_{d_1}\ \mathbf{y}_1 + \mathbf{K}_{d_2}\ \dot{\mathbf{y}}_1$ to $\tilde{\mathbf{w}}$ to obtain the output of the integrator block ($\mathbf{K}_i/s$). Since $\mathbf{K}_i$ is diagonal it is trivial to invert, and knowing the time step and digital integration scheme, we can work backwards to find the error, $\tilde{\mathbf{e}}$, which is the input to the integrator block. *Adding* $\mathbf{y}_1$ to this error we obtain $\tilde{\mathbf{y}}_c$, the commanded modes. We multiply this by $\mathbf{C}$ (eq. (37)) and obtain the desired pilot input, $\tilde{\mathbf{z}}_0$. Using this process we have assured that line 5 of figure 16 would be true.

Comparing line 3 and line 5, we have one input, $\mathbf{z}_0$, which causes saturation ($\tilde{\mathbf{u}}_0$), and another artificial input, $\tilde{\mathbf{z}}_0$, which does not cause saturation ($\mathbf{u}_0$). As before, a binary search is now performed between these two commands to determine an intermediate command, $\mathbf{z}_1'$, which leads to a control vector, $\mathbf{u}_1'$, which is almost, but not quite, saturated. $\mathbf{z}_1'$ and $\mathbf{u}_1'$ become the new controller input and output, respectively, for the next iteration (line 6).

It is obvious that the controller code will have to be cycled many times during one time step in order to perform the binary search while the controls are saturated, whereas, in the absence of saturation, the controller code is cycled only once per time step. This means that additional computational power must be available to handle the control saturation case.

CONTROL SATURATION VALIDATION

The effectiveness of this control-limiting algorithm is dramatically demonstrated by two test cases: the aircraft response to an artificially large angle of attack command input (fig. 17) and the response to an artificially large upward gust with no change in pilot command input (fig. 18).

The large angle-of-attack command pulse (dashed line, curve 6, fig. 17) produces a sudden 2-g loading of the aircraft. The response (curve 1) is not linear, but it is stable. The left and right

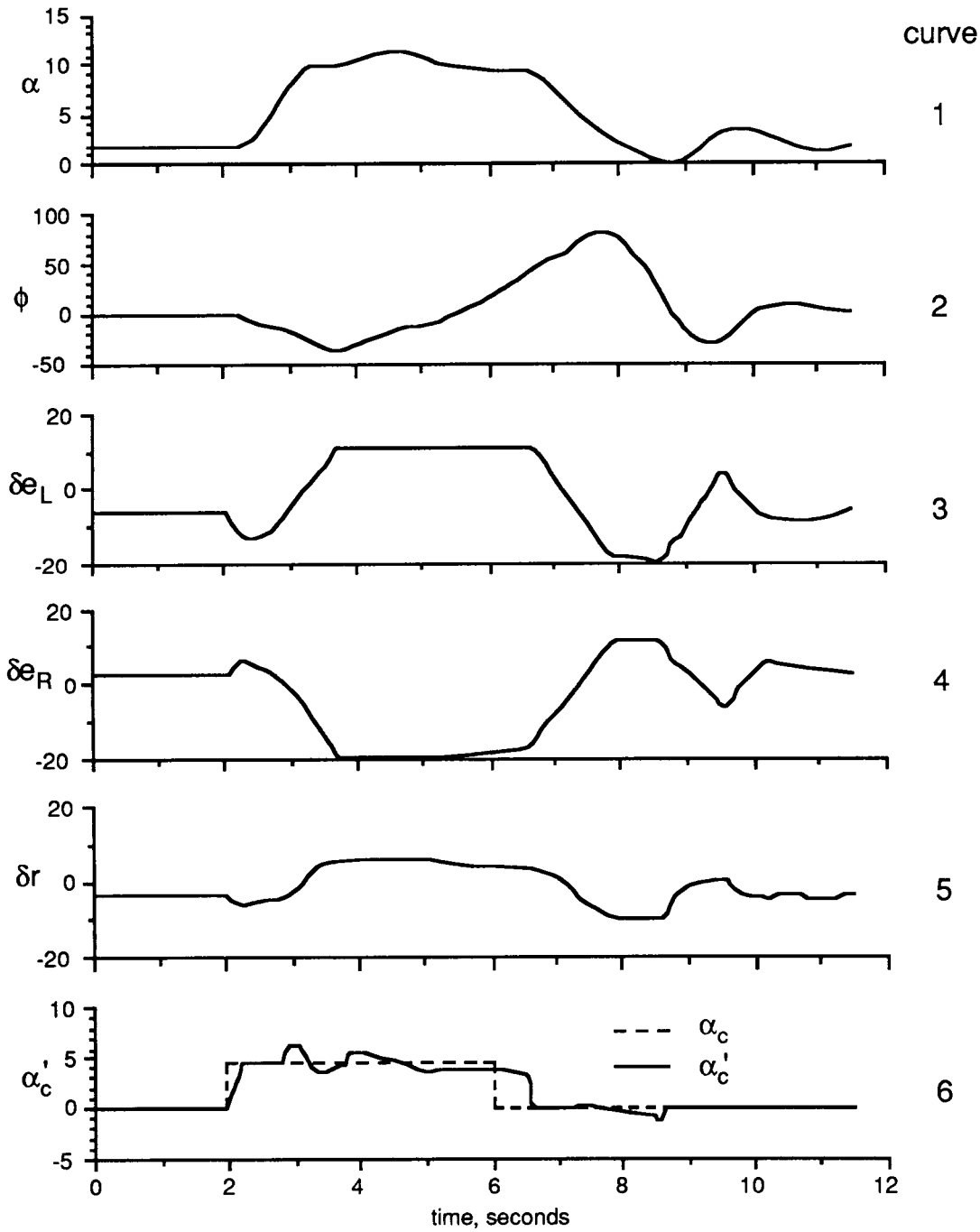

Figure 17. – 2-g angle-of-attack command pulse.

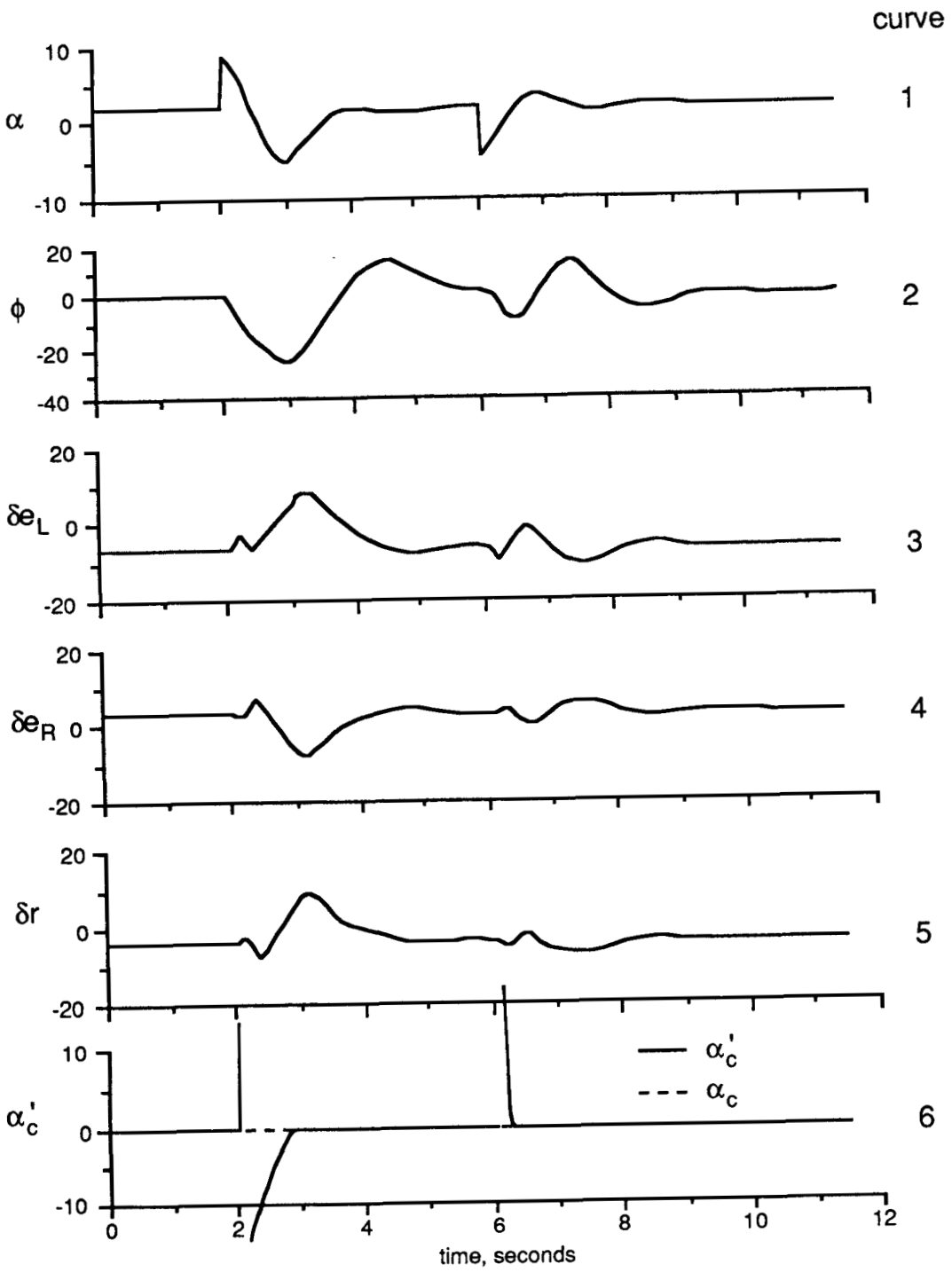

Figure 18. – 100-fps upward gust pulse.

elevator (curves 3 and 4) are rate-limited during the maneuver and the left elevator is position-limited. The solid line in curve 6 shows the restricted angle of attack input (α_c') after the saturation logic has been applied. It deviates from the pulse input (dashed line, curve 6) only when a control is rate- or position-saturated. As you can see, the system returns to linear operation after about 9 sec. Notice that the bank angle (curve 2) returns to zero after this large input.

Figure 18 shows the OWRA response to a 100-fps upward gust pulse at the reference condition. The response (curve 1) is rapid and takes about 2 sec to return to the original angle of attack before the gust. The left and right elevators (curves 3 and 4) are both rate-limited for about 1 sec. Notice that the artificial angle-of-attack command, α_c' (solid line, curve 6), is very large at the time of the gust, but quickly returns to zero as the aircraft responds to the controls. This large input signal balances the gust input so that the error signal doesn't saturate the available controls.

With no change in the limiting logic, the outer roll-angle loop can drive the system unstable during limiting. This is a general problem with cascaded outer loops. The stable response in roll angle (curve 2 in fig. 18) was obtained by suspending the outer loop during control saturation, saving the commanded bank angle at the onset of control saturation, and restarting the outer loop when normal linear operation is achieved. As the reader can see, the steady state roll angle is zero despite a short period of nonlinear operation during the gust.

Using the saturation logic described above, typically one weakest control stays saturated, because it is unlikely that two or more controls would exceed their limits at the same time. In the case of the OWRA, that one weakest control is frequently the left elevator. This suggests that if the left elevator had more control power, that is, the left elevator were larger than the right elevator, the aircraft could maneuver more rapidly than before without exceeding the control limits.

It is not too surprising that the left elevator limits first. With the right wing swept forward, the natural response to a pitch-up command is to pitch up and roll right, until stall of the left wing (see fig. 1). To obtain a pure, decoupled, pitch-up response, the control system will require a pitch-up and roll-left moment. The left elevator provides the correct combination of signs to get these moments, i.e., pitch up and roll left. This again indicates that the left elevator should be larger than the right elevator to provide more rapid maneuvering without control saturation.

If a differential canard is used to generate rolling moments, then with the right wing swept forward, as in the OWRA, the right canard elevator provides a pitch-up moment in combination with a roll-left moment. This indicates that the right canard should be larger than the left canard to provide more rapid maneuvering without control saturation.

Note that in general for oblique-wing aircraft with the right wing swept forward, control surfaces placed aft and left or placed forward and right of the center of gravity will generate the correct combination of moment signs to decouple the short-period natural response.

This idea can be generalized to all oblique wings, regardless of sweep direction, by the following rule. If we divide the aircraft plan view into quadrants about the center of gravity, that is, forward-left, forward-right, aft-left, and aft-right, then control surfaces in the same quadrant as a wing will generate the correct combination of moment signs to decouple the short-period response and should

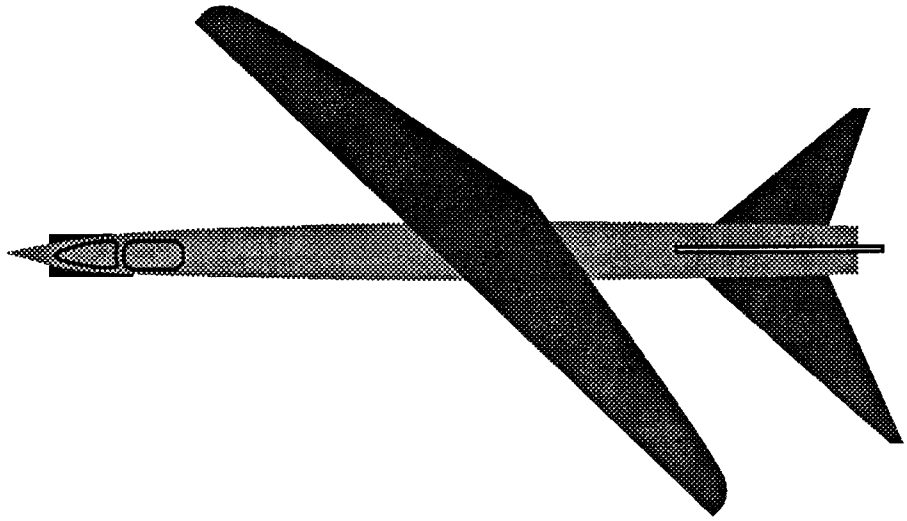

Figure 19. – OWRA at 45° sweep with asymmetric tail.

therefore be larger than surfaces in quadrants without a wing which will tend to aggravate the short-period response. The elevator and canard examples described above conform to this rule. Note also that each wing aileron acting independently produces the correct moment signs and conforms to the above rule.

A possible drawback of using an asymmetric tail on the OWRA is that the asymmetric tail would generate an extraneous rolling moment when used as a pitch control at zero sweep. However, this rolling moment could be overcome by the ailerons which would, at zero sweep, have a much larger lateral moment arm than the elevator. An OWRA with such an asymmetric tail is shown in figure 19.

CONCLUDING REMARKS

A modal control system design technique has been applied to a linear model of the OWRA and tested with a six-degree-of-freedom, nonlinear simulation of the same. This technique was found to have the following desirable characteristics. (1) It allows the direct application of single-input/single-output techniques to multiple-input/multiple-output systems. (2) The control gains have direct physical significance to the natural aircraft modes. (3) The technique provides a decoupled response from a highly coupled system. (4) The closed-loop system has zero steady state error in the presence of loads and noise. (5) This linear control system remains stable while controlling a highly nonlinear natural system. (6) The control saturation logic keeps the system stable when excited by large command inputs and external loads which temporarily saturate the controls.

During the course of this investigation, it became apparent that the aircraft configuration could be improved to make the control system designer's job easier. An asymmetrically sized horizontal

tail in which the surface behind the aft swept wing is larger than its mate would allow more rapid maneuvering without saturating the controls. This asymmetric tail provides moments which are more aligned to control the highly roll-pitch coupled short period mode in oblique-wing aircraft.

Ames Research Center
National Aeronautics and Space Administration
Moffett Field, California 94035, June 21, 1988

APPENDIX A
COMPLEX CONJUGATE EQUATION PAIRS

We wish to examine the relationship between a pair of equations, p and $p+1$, extracted from the complete diagonalized set of equations, equations (3). This pair of equations represents a second-order mode for which we know that the eigenvalues are complex conjugates, $\lambda_{p+1} = \lambda_p^*$ (see eqs. (8)). We wish to show that the second equation is the complex conjugate of the first.

From equations (3) and (4) we can write directly

$$\begin{aligned} \boldsymbol{\xi} &= \mathbf{X}^{-1}\,\mathbf{x} \\ \dot{\boldsymbol{\xi}} &= \boldsymbol{\Lambda}\,\boldsymbol{\xi} + \mathbf{M}\,\mathbf{u} \end{aligned} \tag{A1}$$

Let us define

$$\begin{aligned} \mathbf{X} &= [v_1\ v_2\ \cdots v_n] \\ \mathbf{X}^{-1} &= [\omega_1\ \omega_2\ \cdots \omega_n]^T \\ \mathbf{G} &= [g_1\ g_2\ \cdots g_m] \end{aligned} \tag{A2}$$

where the v_j and g_j are column vectors and the ω_i are row vectors. From equations (3) and knowing that the eigenvalues are complex conjugates, equations p and $p+1$ can be written as

$$\begin{aligned} \dot{\xi}_p &= \lambda_p\,\xi_p + \nu_p \\ \dot{\xi}_{p+1} &= \lambda_p^*\,\xi_{p+1} + \nu_{p+1} \end{aligned} \tag{A3}$$

where, because $\mathbf{M} = \mathbf{X}^{-1}\mathbf{G}$,

$$\begin{aligned} \nu_p &= \sum_{j=1}^{m} \omega_p g_j\,u_j \\ \nu_{p+1} &= \sum_{j=1}^{m} \omega_{p+1} g_j\,u_j \end{aligned} \tag{A4}$$

First we show that the ω_i are the left eigenvectors of $\mathbf{F}$. From the definition of eigenvectors and the matrix $\mathbf{X}$ we can write

$$\mathbf{F}\,v_j = \lambda_j\,v_j \tag{A5}$$

The v_j are called the right eigenvectors because they multiply $\mathbf{F}$ on the right. We can write successively

$$\begin{aligned} \mathbf{F}\mathbf{X} &= \mathbf{X}\boldsymbol{\Lambda} \\ \mathbf{F} &= \mathbf{X}\boldsymbol{\Lambda}\mathbf{X}^{-1} \\ \mathbf{X}^{-1}\mathbf{F} &= \boldsymbol{\Lambda}\mathbf{X}^{-1} \end{aligned} \tag{A6}$$

From equation A6, we can write for each row

$$\omega_i\mathbf{F} = \lambda_i\,\omega_i \tag{A7}$$

The ω_i are called the left eigenvectors because they multiply $\mathbf{F}$ on the left. In particular for row p we can write

$$\omega_p\mathbf{F} = \lambda_p\,\omega_p \tag{A8}$$

Taking the complex conjugate of equation A8 we get successively

$$\begin{aligned}(\omega_p \mathbf{F})^* &= (\lambda_p\, \omega_p)^* \\ \omega_p^* \mathbf{F} &= \lambda_p^*\, \omega_p^*\end{aligned} \tag{A9}$$

But because $\lambda_p^* = \lambda_{p+1}$ and for each eigenvalue there is a unique eigenvector, then

$$\omega_{p+1} = \omega_p^* \tag{A10}$$

Now from the definition of ξ, equations A1 and A2, we can write

$$\begin{aligned}\xi_p &= \omega_p\, x \\ \xi_{p+1} &= \omega_{p+1}\, x\end{aligned} \tag{A11}$$

But $\omega_{p+1} = \omega_p^*$, so we can write

$$\xi_{p+1} = \omega_p^*\, x = \xi_p^* \tag{A12}$$

Using similar logic, we can write successively

$$\begin{aligned}\nu_{p+1} &= \sum_{j=1}^{m} \omega_{p+1} g_j\, u_j \\ &= \sum_{j=1}^{m} \omega_p^* g_j\, u_j \\ &= \sum_{j=1}^{m} (\omega_p g_j)^*\, u_j \\ &= \nu_p^*\end{aligned} \tag{A13}$$

Therefore, the $p + 1$ equation can be written as

$$\xi_p^* = \lambda_p^*\, \xi_p^* + \nu_p^* \tag{A14}$$

APPENDIX B
OWRA SYSTEM MATRICES

This appendix presents in numerical form the system matrices associated with the OWRA at the study condition. Each matrix has a row of symbols across the top and a column of symbols along the side. Each symbol across the top indicates the component of the vector the matrix multiplies. Each symbol down the side indicates the equation corresponding to that row. All numbers are rounded to three decimal places to adequately show the structure of the matrices without inundating the reader in numerical trivia.

The natural-system matrices, **F** and **G** are presented first.

$$\mathbf{F} = \begin{array}{c} \begin{matrix} q & \alpha & u/U_1 & \theta & p & r & \beta & \phi \end{matrix} \\ \left[\begin{array}{cccccccc} -0.996 & -7.054 & 0 & 0 & 0.145 & 0.086 & 0 & 0 \\ 1 & -0.804 & -0.083 & 0 & 0 & 0 & 0 & 0 \\ 0 & 0.026 & -0.015 & -0.039 & 0 & 0 & 0 & 0 \\ 1 & 0 & 0 & 0 & 0 & 0 & 0 & 0 \\ 1.860 & 36.427 & 0 & 0 & -3.117 & 2.087 & -67.201 & 0 \\ 0 & -1.852 & 0 & 0 & 0.040 & -0.710 & 10.833 & 0 \\ 0 & 0 & 0 & 0 & -1 & -0.293 & 0.039 & 0 \\ 0 & 0 & 0 & 0 & 1 & 0 & 0 & 0 \end{array}\right] \end{array} \begin{matrix} M \\ Z \\ X \\ d\theta \\ L \\ N \\ Y \\ d\phi \end{matrix}$$

$$\mathbf{G} = \begin{array}{c} \begin{matrix} \delta e_L & \delta e_R & \delta_r \end{matrix} \\ \left[\begin{array}{ccc} -0.152 & -0.175 & 0.010 \\ -0.002 & -0.002 & 0 \\ 0 & 0 & -0.000 \\ 0 & 0 & 0 \\ 0.206 & -0.355 & 0.266 \\ 0.028 & -0.031 & -0.108 \\ -0.000 & 0.000 & 0.001 \\ 0 & 0 & 0 \end{array}\right] \end{array} \begin{matrix} M \\ Z \\ X \\ d\theta \\ L \\ N \\ Y \\ d\phi \end{matrix}$$

The matrix of eigenvectors, **X**, and its inverse, $\mathbf{X}^{-1}$, are presented next.

$$
\mathbf{X} = \begin{array}{c}
\begin{array}{cccc} & \textit{Dutch Roll} & & \textit{Short Period} \end{array} \\
\left[\begin{array}{cccc}
(0.004, 0.100) & (0.004, -0.100) & (-0.037, 0.351) & (-0.037, -0.351) \\
(0.032, 0.002) & (0.032, -0.002) & (0.134, 0.000) & (0.134, -0.000) \\
(0.000, 0.000) & (0.000, -0.000) & (0.001, 0.000) & (0.001, -0.000) \\
(0.031, -0.006) & (0.031, 0.006) & (0.119, -0.035) & (0.119, 0.035) \\
(-0.631, 0.670) & (-0.631, -0.670) & (0.153, -0.844) & (0.153, 0.844) \\
(0.024, -0.227) & (0.024, 0.227) & (0.088, -0.073) & (0.088, 0.073) \\
(0.074, 0.000) & (0.074, 0.000) & (0.037, 0.027) & (0.037, -0.027) \\
(0.238, 0.164) & (0.238, -0.164) & (-0.296, 0.064) & (-0.296, -0.064)
\end{array}\right]
\end{array}
$$

Roll Mode	*Spiral Mode*	*Phugoid Mode*		
−0.025	−0.000	(0.039, −0.001)	(0.039, 0.001)	M
0.013	−0.000	(−0.006, −0.000)	(−0.006, 0.000)	Z
0.000	0.001	(0.526, 0.000)	(0.526, −0.000)	X
0.009	0.000	(−0.106, −0.719)	(−0.106, 0.719)	$d\theta$
0.939	−0.030	(−0.019, −0.014)	(−0.019, 0.014)	L
−0.011	0.038	(−0.008, 0.015)	(−0.008, −0.015)	N
0.001	0.002	(−0.002, 0.001)	(−0.002, −0.001)	Y
−0.342	0.999	(−0.206, 0.387)	(−0.206, −0.387)	$d\phi$

$$
\mathbf{X}^{-1} = \begin{array}{c}
\begin{array}{cccc} q & \alpha & U/U_1 & \theta \end{array} \\
\left[\begin{array}{cccc}
(-0.672, 0.571) & (-2.137, -1.890) & (0.040, -0.062) & (0.001, 0.000) \\
(-0.672, -0.571) & (-2.137, 1.890) & (0.040, 0.062) & (0.001, -0.000) \\
(0.021, -1.706) & (4.575, 0.293) & (0.043, 0.127) & (-0.001, 0.001) \\
(0.021, 1.706) & (4.575, -0.293) & (0.043, -0.127) & (-0.001, -0.001) \\
3.012 & -7.568 & -0.228 & -0.003 \\
1.397 & 0.077 & 0.414 & 0.537 \\
(-0.002, 0.084) & (-0.005, -0.619) & (0.950, 0.126) & (-0.001, 0.695) \\
(-0.002, -0.084) & (-0.005, 0.619) & (0.950, -0.126) & (-0.001, -0.695)
\end{array}\right]
\end{array}
$$

p	r	β	ϕ	
(−0.002, 0.036)	(−0.325, 2.480)	(7.814, 0.592)	(−0.007, −0.095)	dr
(−0.002, −0.036)	(−0.325, −2.480)	(7.814, −0.592)	(−0.007, 0.095)	dr
(−0.058, −0.048)	(−0.120, −0.869)	(−2.441, −0.259)	(0.009, 0.032)	sp
(−0.058, 0.048)	(−0.120, 0.869)	(−2.441, 0.259)	(0.009, −0.032)	sp
1.231	4.780	12.580	−0.177	rm
0.396	2.438	−0.711	0.921	spl
(−0.000, 0.004)	(−0.003, 0.024)	(0.002, −0.001)	(−0.001, −0.001)	ph
(−0.000, −0.004)	(−0.003, −0.024)	(0.002, 0.001)	(−0.001, 0.001)	ph

Note that for second-order modes, the adjacent columns of $\mathbf{X}$ are complex conjugates whereas adjacent rows of $\mathbf{X}^{-1}$ are complex conjugates.

The diagonal eigenvalue matrix, $\mathbf{\Lambda}$, is presented next. Note that the second-order modes have complex eigenvalues.

$$\mathbf{\Lambda} = \begin{bmatrix} (-0.487, 3.146) & 0 & 0 & 0 \\ 0 & (-0.487, -3.146) & 0 & 0 \\ 0 & 0 & (-1.084, 2.618) & 0 \\ 0 & 0 & 0 & (-1.084, -2.618) \\ 0 & 0 & 0 & 0 \\ 0 & 0 & 0 & 0 \\ 0 & 0 & 0 & 0 \\ 0 & 0 & 0 & 0 \end{bmatrix}$$

$$\begin{bmatrix} 0 & 0 & 0 & 0 \\ 0 & 0 & 0 & 0 \\ 0 & 0 & 0 & 0 \\ 0 & 0 & 0 & 0 \\ -2.750 & 0 & 0 & 0 \\ 0 & -0.030 & 0 & 0 \\ 0 & 0 & (-0.007, 0.053) & 0 \\ 0 & 0 & 0 & (-0.007, -0.053) \end{bmatrix} \begin{matrix} dr \\ dr \\ sp \\ sp \\ rm \\ spl \\ ph \\ ph \end{matrix}$$

The complex modal control matrix, $\mathbf{M}$, is presented next. Note that the rows corresponding to second-order modes are complex conjugates of each other as shown in appendix A.

$$\mathbf{M} = \begin{matrix} \delta e_L \\ \\ \\ \\ \\ \\ \\ \\ \end{matrix} \begin{matrix} \delta e_R \\ \\ \\ \\ \\ \\ \\ \\ \end{matrix} \begin{matrix} \delta_r \\ \\ \\ \\ \\ \\ \\ \\ \end{matrix}$$

$$\begin{bmatrix} (0.094, -0.007) & (0.134, -0.186) & (0.037, -0.253) \\ (0.094, 0.007) & (0.134, 0.186) & (0.037, 0.253) \\ (-0.026, 0.225) & (0.012, 0.341) & (-0.005, 0.064) \\ (-0.026, 0.225) & (0.012, 0.341) & (-0.005, 0.064) \\ -0.062 & -1.094 & -0.147 \\ -0.063 & -0.460 & -0.147 \\ (0.000, -0.010) & (0.001, -0.016) & (0.000, -0.001) \\ (0.000, 0.010) & (0.001, 0.016) & (0.000, 0.001) \end{bmatrix} \begin{matrix} dr \\ dr \\ sp \\ sp \\ rm \\ spl \\ ph \\ ph \end{matrix}$$

Using the rule established in equation (10) for each second-order mode, we can develop the second-order transformation matrix, $\mathbf{P}^{-1}$.

$$\mathbf{P}^{-1} = \begin{bmatrix} (0.487, 3.146) & (0.487, -3.146) & 0 & 0 \\ 1 & 1 & 0 & 0 \\ 0 & 0 & (1.084, 2.618) & (-1.084, -2.618) \\ 0 & 0 & 1 & 1 \\ 0 & 0 & 0 & 0 \\ 0 & 0 & 0 & 0 \\ 0 & 0 & 0 & 0 \\ 0 & 0 & 0 & 0 \end{bmatrix}$$

$$\begin{bmatrix} 0 & 0 & 0 & 0 \\ 0 & 0 & 0 & 0 \\ 0 & 0 & 0 & 0 \\ 0 & 0 & 0 & 0 \\ 1 & 0 & 0 & 0 \\ 0 & 1 & 0 & 0 \\ 0 & 0 & (0.007, 0.053) & (0.007, -0.053) \\ 0 & 0 & 1 & 1 \end{bmatrix} \begin{matrix} dr \\ dr \\ sp \\ sp \\ rm \\ spl \\ ph \\ ph \end{matrix}$$

$\mathbf{P}$ is just the inverse of $\mathbf{P}^{-1}$. Note that $\mathbf{P}$ has the same structure as $\mathbf{P}^{-1}$, that is, 1's opposite real eigenvalues and block 2×2 matrices opposite complex conjugate eigenvalues. In practice, it is never actually necessary to calculate $\mathbf{P}$.

$$\mathbf{P} = \begin{bmatrix} (0, -0.159) & (0.5, 0.077) & 0 & 0 \\ (0, 0.159) & (0.5, -0.077) & 0 & 0 \\ 0 & 0 & (0, -0.191) & (0.5, 0.207) \\ 0 & 0 & (0, 0.191) & (0.5, -0.207) \\ 0 & 0 & 0 & 0 \\ 0 & 0 & 0 & 0 \\ 0 & 0 & 0 & 0 \\ 0 & 0 & 0 & 0 \end{bmatrix}$$

$$\begin{bmatrix} 0 & 0 & 0 & 0 \\ 0 & 0 & 0 & 0 \\ 0 & 0 & 0 & 0 \\ 0 & 0 & 0 & 0 \\ 1 & 0 & 0 & 0 \\ 0 & 1 & 0 & 0 \\ 0 & 0 & (0, -9.461) & (0.5, 0.066) \\ 0 & 0 & (0, 9.461) & (0.5, -0.066) \end{bmatrix} \begin{matrix} dr \\ dr \\ sp \\ sp \\ rm \\ spl \\ ph \\ ph \end{matrix}$$

Proceeding with the analysis, we calculate $\mathbf{\Gamma}$ as $\mathbf{P}^{-1}\mathbf{\Lambda}\mathbf{P}$. Note that $\mathbf{\Gamma}$ is real with the structure of equation (11) opposite complex conjugate eigenvalues.

$$\mathbf{\Gamma} = \begin{bmatrix} 0 & -10.135 & 0 & 0 & 0 & 0 & 0 & 0 \\ 1 & -0.973 & 0 & 0 & 0 & 0 & 0 & 0 \\ 0 & 0 & 0 & -8.030 & 0 & 0 & 0 & 0 \\ 0 & 0 & 1 & -2.167 & 0 & 0 & 0 & 0 \\ 0 & 0 & 0 & 0 & -2.750 & 0 & 0 & 0 \\ 0 & 0 & 0 & 0 & 0 & -0.030 & 0 & 0 \\ 0 & 0 & 0 & 0 & 0 & 0 & 0 & -0.003 \\ 0 & 0 & 0 & 0 & 0 & 0 & 1 & -0.014 \end{bmatrix} \begin{matrix} dr \\ dr \\ sp \\ sp \\ rm \\ spl \\ ph \\ ph \end{matrix}$$

The second-order modal control matrix $\mathbf{S}$ is just $\mathbf{P}^{-1}\mathbf{M}$. Note that $\mathbf{S}$ is a real matrix.

$$\mathbf{S} = \begin{matrix} \\ \\ \\ \\ \\ \\ \\ \\ \end{matrix} \begin{matrix} \delta e_L \\ \end{matrix} \begin{matrix} \delta e_R \\ \end{matrix} \begin{matrix} \delta_r \\ \end{matrix} \begin{bmatrix} 0.139 & 1.299 & 1.626 \\ 0.188 & 0.268 & 0.074 \\ -1.234 & -1.762 & -0.347 \\ -0.052 & 0.024 & -0.010 \\ -0.062 & -1.094 & -0.147 \\ -0.063 & -0.460 & -0.146 \\ 0.001 & 0.002 & 0.000 \\ 0.000 & 0.001 & 0.000 \end{bmatrix} \begin{matrix} dr \\ dr \\ sp \\ sp \\ rm \\ spl \\ ph \\ ph \end{matrix}$$

To transform directly from the open-loop system, equations (3), to the transformed modal system, equation (6), we need the real transformation matrix, $\mathbf{T}^{-1}$. This is just the product of the two previous transformation matrices, that is, $\mathbf{T}^{-1} = \mathbf{P}^{-1}\mathbf{X}^{-1}$.

$$\mathbf{T}^{-1} = \begin{matrix} \\ \\ \\ \\ \\ \\ \\ \\ \end{matrix} \begin{matrix} q \\ \end{matrix} \begin{matrix} \alpha \\ \end{matrix} \begin{matrix} u/U_1 \\ \end{matrix} \begin{matrix} \theta \\ \end{matrix} \begin{matrix} p \\ \end{matrix} \begin{matrix} r \\ \end{matrix} \begin{matrix} \beta \\ \end{matrix} \begin{matrix} \phi \\ \end{matrix} \begin{bmatrix} -4.248 & 9.813 & 0.430 & -0.002 & -0.227 & -15.923 & 3.882 & 0.590 \\ -1.344 & -4.273 & 0.081 & 0.002 & -0.004 & -0.649 & 15.628 & -0.015 \\ 8.981 & 8.381 & -0.572 & -0.009 & 0.126 & 4.293 & -3.935 & -0.148 \\ 0.043 & 9.150 & 0.085 & -0.003 & -0.116 & -0.240 & -4.882 & 0.019 \\ 3.012 & -7.568 & -0.228 & -0.003 & 1.231 & 4.780 & 12.580 & -0.177 \\ 1.397 & 0.077 & 0.414 & 0.537 & 0.396 & 2.438 & -0.711 & 0.921 \\ -0.009 & 0.065 & -0.000 & -0.073 & -0.000 & -0.003 & 0.000 & 0.000 \\ -0.004 & -0.010 & 1.890 & -0.001 & -0.001 & -0.005 & 0.004 & -0.002 \end{bmatrix} \begin{matrix} dr \\ dr \\ sp \\ sp \\ rm \\ spl \\ ph \\ ph \end{matrix}$$

$\mathbf{T}$ is just the inverse of $\mathbf{T}^{-1}$

$$\mathbf{T} = \begin{array}{c} \begin{matrix} dr & dr & sp & sp & rm & spl & ph & ph \end{matrix} \\ \begin{bmatrix} 0.032 & -0.011 & 0.134 & -0.183 & -0.025 & -0.000 & -0.011 & 0.039 \\ 0.001 & 0.031 & 0.000 & 0.134 & 0.013 & -0.000 & -0.006 & -0.006 \\ 0.000 & 0.000 & 0.000 & 0.001 & 0.000 & 0.001 & 0.000 & 0.526 \\ -0.002 & 0.032 & -0.013 & 0.134 & 0.009 & 0.000 & -13.609 & -0.011 \\ 0.213 & -0.735 & -0.322 & 0.503 & 0.939 & -0.030 & -0.257 & -0.017 \\ -0.072 & 0.059 & -0.028 & 0.118 & -0.011 & 0.038 & 0.280 & -0.009 \\ 0.000 & 0.074 & 0.010 & 0.026 & 0.001 & 0.002 & 0.017 & -0.002 \\ 0.052 & 0.213 & 0.024 & -0.322 & -0.342 & 0.999 & 7.325 & -0.257 \end{bmatrix} \end{array} \begin{matrix} q \\ \alpha \\ u/U_1 \\ \theta \\ p \\ r \\ \beta \\ \phi \end{matrix}$$

REFERENCES

1. Alag, Gurbux S.; Kempel, Robert W.; and Pahle, Joseph W.: Decoupling Control Synthesis for an Oblique-Wing Aircraft. NASA TM 86801, 1986.

2. Alag, Gurbux S.; Kempel, Robert W.; Pahle, Joseph W.; Bresina, John J.; and Bartoli, Febo: Model-Following Control for an Oblique-Wing Aircraft. NASA TM 88269, 1986.

3. Andry, Jr., Albert. N.; Shapiro, E. Y.; and Chung, Jonathon C.: Eigenstructure Assignment for Linear Systems. IEEE Transactions on Aerospace and Electronic Systems, vol. AES-19, no. 5, 1983, pp. 711-729.

4. Larson, Gregory L.; and Williston, Kenneth W.: Eigenstructure Synthesis of an Oblique Wing Flight Control System. Proceedings of the 24th IEEE Conference on Decision and Control, Fort Lauderdale, Florida, vol. 1, 1985, pp. 660-662.

5. Enns, Dale F.; Bugajski, Dan; and Klepl, Martin: Flight Control for the F-8 Oblique Wing Research Aircraft. 1987 American Control Conference, Minneapolis, Minnesota, vol. 2, 1987, pp. 1112-7.

6. Porter, Brian; and Crossley, Roger: Modal Control Theory and Applications. Taylor & Francis Ltd., 1972.

7. Military Specification, Flying Qualities of Piloted Airplanes, MIL-F-8785C, 1980.

8. Phelan, Richard M.: Automatic Control Systems. Cornell University Press, 1977.

9. Kempel, Robert W.; McNeill, Walter E.; Gilyard, Glenn B.; and Maine, Trindle A.: A Piloted Evaluation of an Oblique-Wing Research Aircraft Motion Simulation With Decoupling Control Laws. NASA TP 2874, 1988.

NASA
National Aeronautics and Space Administration

Report Documentation Page

1. Report No.	2. Government Accession No.	3. Recipient's Catalog No.
NASA TP-2898		

4. Title and Subtitle	5. Report Date
Modal Control of an Oblique Wing Aircraft	January 1989
	6. Performing Organization Code

7. Author(s)	8. Performing Organization Report No.
James D. Phillips	A-88250
	10. Work Unit No.
	505-60

9. Performing Organization Name and Address	11. Contract or Grant No.
Ames Research Center Moffett Field, CA 94035	
	13. Type of Report and Period Covered
12. Sponsoring Agency Name and Address	Technical Paper
National Aeronautics and Space Administration Washington, DC 20546-0001	14. Sponsoring Agency Code

15. Supplementary Notes

Point of Contact: James D. Phillips, Ames Research Center, MS 237-11, Moffett Field, CA 94035
(415) 694-4126 or FTS 464-4126

16. Abstract

A linear modal control algorithm is applied to the NASA Oblique Wing Research Aircraft (OWRA). The control law is evaluated using a detailed nonlinear flight simulation. It is shown that the modal control law attenuates the coupling and nonlinear aerodynamics of the oblique wing and remains stable during control saturation caused by large command inputs or large external disturbances. The technique controls each natural mode independently allowing single-input/single-output techniques to be applied to multiple-input/multiple-output systems.

17. Key Words (Suggested by Author(s))	18. Distribution Statement
Oblique wing, Modal control Linear control Flight dynamics	Unclassified-Unlimited Subject Category – 08

19. Security Classif. (of this report)	20. Security Classif. (of this page)	21. No. of pages	22. Price
Unclassified	Unclassified	52	A04

NASA FORM 1626 OCT 86 For sale by the National Technical Information Service, Springfield, Virginia 22161

NASA-Langley, 1989